Synchronous Ensembles of Hippocampal CA1 Pyramidal Neurons Associated with Theta but not Ripple Oscillations During Novel Exploration

En-Li Chen[1,2], Tsai-Wen Chen[1,2], Eric R. Schreiter[3], Bei-Jung Lin[1,2*]

[1]Institute of Neuroscience, National Yang Ming Chiao Tung University, Taipei, Taiwan
[2]Brain Research Center, National Yang Ming Chiao Tung University, Taipei, Taiwan
[3]Janelia Research Campus, Howard Hughes Medical Institute, Ashburn, VA 20147, USA.
*Corresponding author: beijunglin@nycu.edu.tw

Abstract

Synchronous neuronal ensembles play a pivotal role in the consolidation of long-term memory in the hippocampus. However, their organization during the acquisition of spatial memory remains less clear. In this study, we used neuronal population voltage imaging to investigate the synchronization patterns of CA1 pyramidal neuronal ensembles during the exploration of a new environment, a critical phase for spatial memory acquisition. We found synchronous ensembles comprising approximately 40% of CA1 pyramidal neurons, firing simultaneously in brief windows (~25ms) during immobility and locomotion in novel exploration. Notably, these synchronous ensembles were not associated with ripple oscillations but were instead phase-locked to local field potential theta waves. Specifically, the subthreshold membrane potentials of neurons exhibited coherent theta oscillations with a depolarizing peak at the moment of synchrony. Among newly formed place cells, pairs with more robust synchronization during locomotion displayed more distinct place-specific activities. These findings underscore the role of synchronous ensembles in coordinating place cells of different place fields.

Introduction

The establishment of long-term memory involves the initial acquisition and subsequent consolidation of memory traces, processes intricately connected to the modification of synaptic transmission[1,2]. Synchronous ensembles, characterized by the simultaneous firing of multiple neurons over tens of milliseconds (referred to as population synchrony), play a pivotal role in influencing synaptic plasticity[3-5]. The hippocampus, a crucial region for long-term memory formation[6,7], has been a focal point of synchronous ensemble studies. Within the hippocampus, synchronous ensembles are hypothesized to play roles in reactivating and consolidating labile memory traces[8]. However, their organization during memory acquisition remains less understood.

In the hippocampus, synchronous ensembles among CA1 pyramidal cells (CA1PCs) are predominantly observed during sharp-wave ripples, the brain waves associated with memory consolidation[8-13]. During these events, 10-18% of CA1PCs generate spikes, particularly during offline consummatory behavioral states or sleep[14,15]. These synchronous ensembles are biased toward experience-dependent reactivation, consolidating labile memory traces[16,17]. Furthermore, synchronous ensembles firing action potentials in short windows of 10-30 milliseconds enhance information processing[6] and discriminate distinct behavioral contingencies[18]. Although synchronous ensembles of CA1PCs during offline memory consolidation are well-characterized, their organization during online acquisition of spatial memory, such as when animals enter a new environment and new place cells form, remains unclear.

Previous studies have identified correlated activities among place cells during theta oscillation, where 1-3% of place cells' spikes co-activate in a forward order matching animals' trajectory in the theta cycles when animals' locations overlap in the place fields of these cells[19-21]. Because these place cells fire at distinct theta phases in the same cycle, this coordinated firing operates on the timescale of theta periods (~125ms)[22,23]. Population synchrony on shorter timescales (10-30 ms) is

53 speculated to be reduced by the presence of theta oscillations[22].

54

55 The subthreshold membrane voltage (subVm), influenced by synaptic inputs and intrinsic
56 conductances, directly triggers spiking activity[24,25]. Additionally, properties of subVm support the
57 organization of neuronal representation[26]. Although correlated membrane potentials have been
58 proposed to underlie the synchrony of neuronal ensembles[27,28], multicellular recordings of subVms
59 have not yet provided direct experimental evidence. Given the intricate interaction among subVm,
60 spiking, and place cell formation, it is crucial to investigate the temporal relationships of sub- and
61 suprathreshold neuronal activities among CA1PCs during novel exploration.

62

63 In this study, we used voltage imaging to investigate the temporal dynamics of sub- and
64 suprathreshold neuronal activities in CA1PCs during novel exploration. We found synchronous
65 ensembles involving approximately 40% of CA1PCs exhibited transient population synchrony and
66 correlated subthreshold membrane potentials when mice ran and stopped in a new maze.
67 Surprisingly, these synchronous ensembles occurred outside ripple episodes and were phase-locked
68 to extracellular and intracellular theta oscillations. Notably, cell pairs with stronger synchronous
69 activities established more distinct place fields that overlapped less. In essence, synchronous
70 ensembles facilitated temporal association among place cells representing diverse features of
71 spatial memory. This plastic network, driven by synchronous ensembles, may contribute to the
72 stabilization of place cells, establishing place fields that effectively tile the environment.

73

74 Results

75 To investigate the temporal relationships between neuronal activities during novel exploration, we
76 simultaneously recorded many neurons as animals explored a new environment for the first time.
77 To achieve this, we employed voltage imaging in conjunction with an air-lifted plastic track that
78 allowed mice to explore an environment while remaining head-fixed under a microscope (Figure

1A). To ensure a genuinely novel experience, all pre-training and habituation were performed in a separate room distinct from the one where the imaging experiments were conducted. On the day of imaging, the mice were introduced to the recording room for the first time and initially confined to a specific corner of the track (Figure 1A top view). Subsequently, as the imaging session commenced, the confinement was lifted, granting mice the freedom to explore the track while imaging was conducted.

In novel exploration, mice moved at a speed of 8.3±0.9 cm/s during locomotion (speed>3 cm/s) and spent 53±7% and 36±6% of their time in locomotion and immobility (speed<1 cm/s), respectively (n=5 mice). Meanwhile, they completed 10±2.5 laps during the 180-s imaging periods (n=5 mice).

For voltage imaging, we expressed the voltage indicator Voltron2[29] in CA1 pyramidal cells (CA1PCs) that were born on embryonic day (E) 14.5, allowing us to measure both suprathreshold and subthreshold membrane potentials from multiple CA1PCs (14±4 cells imaged per field of view (mean±s.d.) and, in total, 71 cells imaged from 5 fields of view in 5 mice; Figure 1B, Supplementary Figure 1A, 1B). Simultaneously, we monitored the animals' positions and speed within the track while recording the local field potential (LFP) from the contralateral side of the hippocampus. Consistent with previous studies, neurons labeled on E14.5 located more on the deep side of the pyramidal layer than those labeled on E17.5 ($t_{(601)}$=22.8, p<0.0001, Student's t-test; Supplementary Figure 1C, D)[30-34].

The mean firing rates of cells ranged from 2.3 to 4.3 Hz (25th-75th percentiles) with a median of 3.2 Hz (n=71 cells, Supplementary Figure 2A). Additionally, most CA1PCs exhibited elevated mean firing rates during immobility relative to locomotion, and their firing rates showed a negative correlation with the animals' speed (Supplementary Figure 2B, 2C), consistent with previous research[35].

Synchronous ensembles among many CA1 pyramidal neurons

Figure 1C shows the fluorescence traces of all neurons in a session as an example. Instances of synchronous activity, where many neurons emitted spikes within a narrow time window, were frequently observed (Figure 1C). To investigate synchronous activity within the neuronal population, we selected a reference cell and counted the number of spikes across all other cells that were aligned with the spikes of the reference cell. This approach yielded a grand average cross-correlogram (CCG) capable of elucidating the timing of spikes from the reference cell relative to the combined spikes of the rest of the population. Notably, the grand average CCG exhibited heightened spike counts around zero lags, unlike flattened counts calculated from randomly selected cells of different sessions (Figure 1D and 1E). The full width at half maximum (FWHM) of the peak in the grand average CCG measured 23±14 ms (mean±s.d., n=71 cells from 5 sessions; Figure 1F), indicating the timescale of the population synchrony. Furthermore, pairwise CCGs of many cell pairs showed significant peaks compared to jittered data (percentage of significant pairs: 63% (median) n=497 pairs, Figure 1-figure supplement 1A and 1B). Among pairs with significant peaks, the absolute values of the peak lags ranged from 0.8 to 4.3 ms (25th-75th percentiles) with a median of 2.1 ms, and the FWHM of the peaks ranged from 20 to 46 ms (25th-75th percentiles) with a median of 30 ms (n=315 pairs, Figure 1-figure supplement 1C and 1D). These results highlight the synchronous spiking between neurons on the millisecond timescale.

To systematically reveal individual synchronous events, we counted the number of spikes from all simultaneously recorded neurons within sliding windows of 25 ms. To compare the summed spikes with controls, we randomly jittered the spike trains to perturb spike timings while maintaining spike rates. We identified moments of population synchrony when spike sums exceeded the average of the jittered spike sums plus four standard deviations (Figure 1C). Using the same criterion for event detection, we observed over a 7.8-fold increase in synchronous events in the original data

130 compared to jittered controls (mean event rate: 0.94±0.17 Hz for the original data, 0.12±0.01 Hz for
131 the jittered data, n=10 segments, p=0.002, W=55, Wilcoxon signed-rank test; Figure 1G). The
132 observed population synchrony was not attributable to spikes in complex bursts, as synchronous
133 event rates did not differ significantly with or without the inclusion of later spikes in bursts
134 (Supplementary Figure 3). Furthermore, we calculated the percentage of neurons participating in
135 these synchronous events to examine the synchronous ensemble sizes. The ensemble sizes ranged
136 from 32% to 53% (25th-75th percentiles) with a median of 42%, which were larger than the
137 synchronous ensemble sizes associated with ripples[14] (Figure 1H). These results demonstrate
138 synchronous ensembles of CA1PCs engaging many neurons.
139

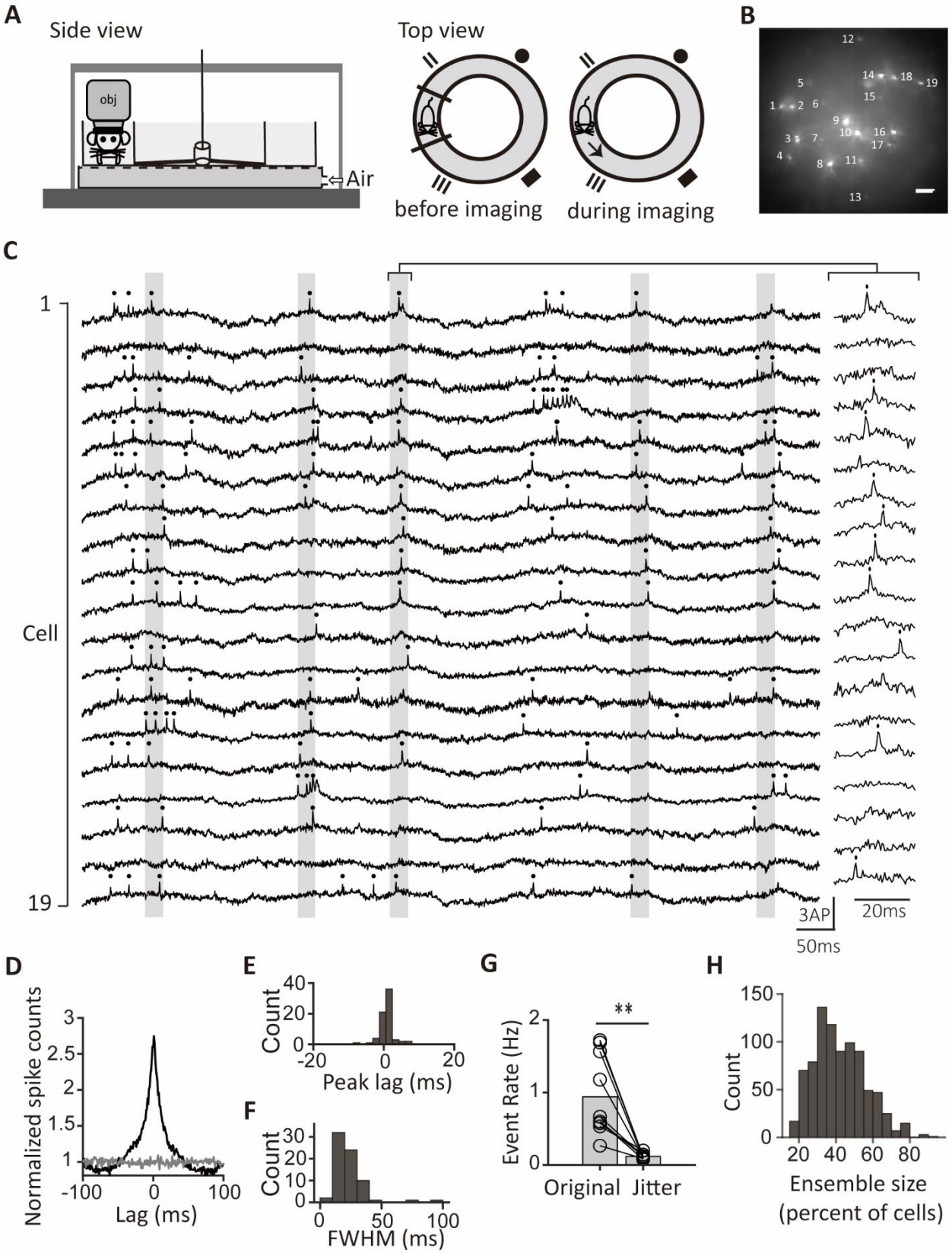

Figure 1. Population synchrony during novel exploration.

(A) Schematic of the behavioral setup for voltage imaging. Mice explored a novel one-way track

143 while fluorescence images were captured at the CA1 pyramidal layer. Left: side view; right: top view
144 of the setup.
145 **(B)** Example time-averaged image of CA1 pyramidal cells expressing Voltron2-ST labeled with JF_{552}-
146 HaloTag ligand. Scale bar, 100 μm.
147 **(C)** Fluorescence traces of cells in an example session with identified synchronous ensembles
148 (labeled with gray vertical bars). Right: an example of magnified fluorescence traces within the
149 bracket, pinpointing the occurrence of the identified synchronous ensemble. Spikes are indicated by
150 dots on the top.
151 **(D)** The grand average cross-correlogram (CCG) averaged across all 71 cells. The gray line represents
152 the mean grand average CCG between reference cells and randomly selected cells from different
153 sessions.
154 **(E)** Distribution of the grand average CCG peak lags of all cells (n=71).
155 **(F)** Distribution of the full width at half maximum (FWHM) of the grand average CCGs (n=71 cells).
156 **(G)** Pairwise comparison of the event rates of population synchrony between original and jittered
157 data. Bar heights indicate group means. **p<0.01
158 (**H**) Histogram of the ensemble sizes as percentages of cells participating in the synchronous
159 ensembles.
160
161
162 **Synchronous ensembles during locomotion and immobility of novel exploration**
163 The hippocampus exhibits state-dependent activities when rodents are engaged in locomotion and
164 immobility[35,36]. In novel exploration, CA1PCs showed synchronous spiking during locomotion and
165 immobility (Figure 2A). To investigate whether these synchronous activities differed between these
166 behavioral states, we compared grant average CCGs and synchronous ensembles under these
167 conditions. During both immobility and locomotion, grant average CCGs showed prominent peaks
168 compared to jittered data (Figure 2B). Moreover, synchronous ensembles were rich in both

immobility and locomotion periods (Figure 2A, 2B and 2D). Nevertheless, the FWHMs of grant average CCGs were broader in the immobility group compared to the locomotion group (Figure 2B and 2C). Synchronous events occurred more frequently during immobility compared to locomotion (Figure 2D). Additionally, ensemble sizes were significantly larger in the immobility group compared to the locomotion group (Figure 2E). Taken together, with differences in sizes and kinetics, there were synchronous ensembles during both immobility and locomotion periods of novel exploration.

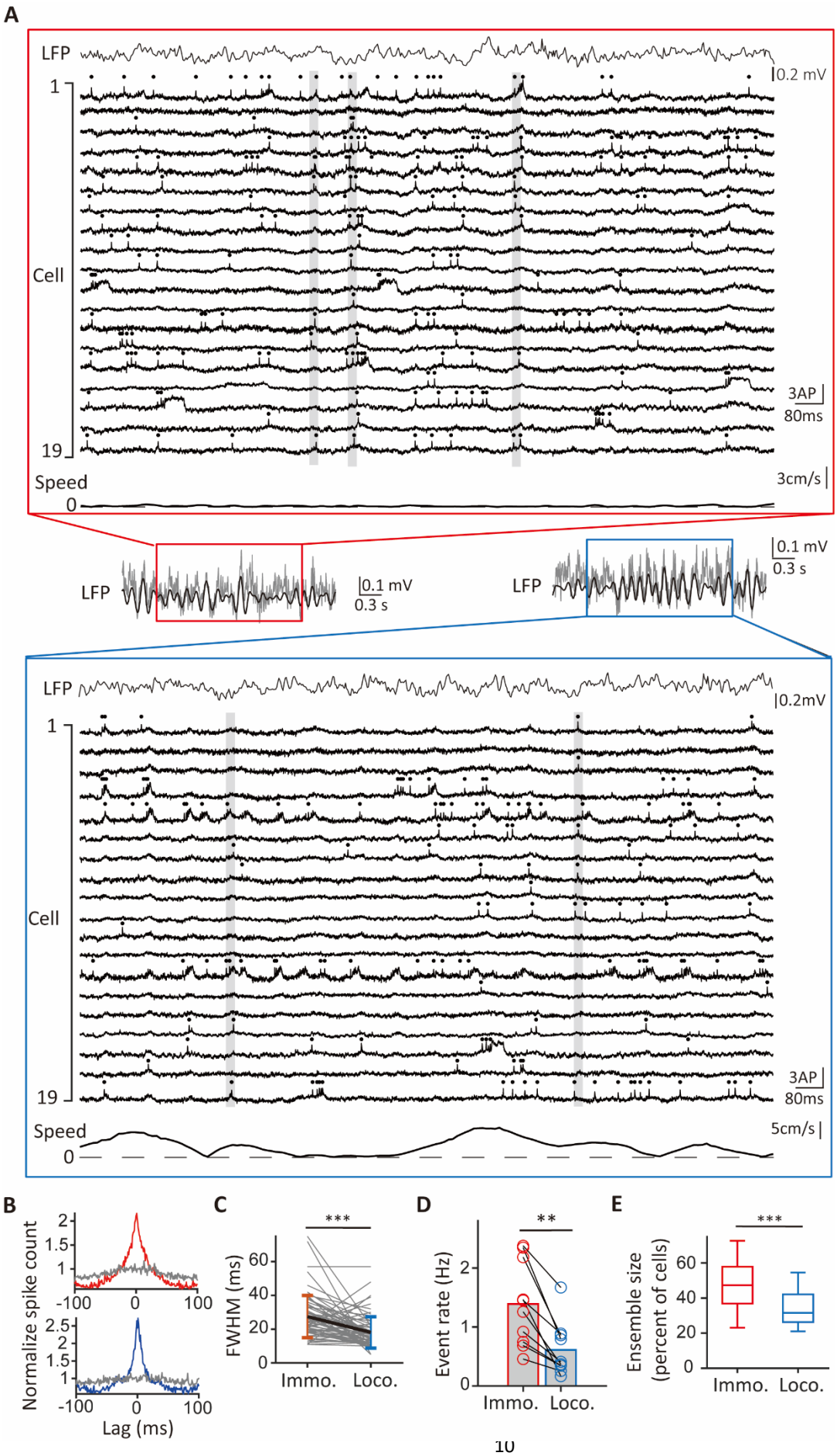
A
LFP
0.2 mV
1
Cell
19
3AP
80ms
Speed
0
3cm/s
LFP
0.1 mV
0.3 s
LFP
0.1 mV
0.3 s
LFP
0.2mV
1
Cell
19
3AP
80ms
Speed
0
5cm/s
B
Normalize spike count
Lag (ms)
C
FWHM (ms)
Immo.
Loco.
D
Event rate (Hz)
Immo.
Loco.
E
Ensemble size (percent of cells)
Immo.
Loco.

175

176 **Figure 2. Comparison of synchronous ensembles between immobility and locomotion.**

177 **(A)** Example traces of cells in a session with identified synchronous ensembles (gray vertical bars)
178 during periods of immobility (red rectangular frame) and locomotion (blue rectangular frame).
179 Spikes are indicated by dots at the top of individual traces. Top: the simultaneously recorded LFP
180 trace. Bottom: simultaneously recorded speed of the animal. Inset: the band-pass filtered LFP trace
181 at the theta frequency range (black line) overlaid on the raw LFP trace (gray line).

182 **(B)** The grand average cross-correlograms (CCGs) during immobility (red) and locomotion (blue)
183 averaged across all cells (n=71). The gray lines represent the mean grand average CCGs calculated
184 from jittered data.

185 **(C)** Pairwise comparison of peak widths (FWHM) in the grand average CCGs between immobility
186 (red) and locomotion (blue). Vertical bars represent means and standard deviations for both groups
187 (FWHM: 27±12 ms for immobility, 18±9 ms for locomotion, mean±s.d., $t_{(70)}$=5.45, p<0.001, paired
188 Student's t-test, n=71 cells). ***p<0.001

189 **(D)** Pairwise comparison of event rates of population synchrony during immobility and locomotion.
190 Bar heights indicate group means (immobility: 1.4±0.7 Hz, locomotion: 0.6±0.5 Hz, mean±s.d., n=10
191 segments, W=55, p=0.002, Wilcoxon signed-rank test). **p<0.01

192 **(E)** Boxplot of ensemble sizes for synchronous ensembles occurring during immobility (red) and
193 locomotion (blue) (median ensemble size: 47% for immobility, n=446 events, 32% for locomotion,
194 n=313 events, $t_{(757)}$=13.54, p<0.001, Student's t-test). ***p<0.001

195

196

197 Synchronous ensembles occur outside ripple episodes

198 CA1PCs exhibit synchronous activities when the hippocampal network emits ripple waves[8,14]. To test
199 whether there is a co-occurrence of synchronous ensembles and ripples, we first detected ripples
200 from LFP recordings. Ripples were detected in three of the five recording sessions, and all occurred
201 during immobility (mean ripple rate: 0.04±0.02 Hz during immobility, 0 Hz during locomotion). In

202 the two recording sessions where we did not detect any ripples, we verified the recording quality of
203 the LFP signal by running multiple tests after the recording sessions. Ripples were identified in the
204 same animals during quality tests, indicating that the absence of ripples during novel immobility in
205 the recording session was not due to the deterioration of LFP recordings (Figure 3-figure
206 supplement 1).
207
208 To visualize both ripples and synchronous ensembles, we plotted voltage traces of neurons
209 alongside simultaneously recorded ripple oscillations. It was typical for synchronous ensembles to
210 occur far away from ripple episodes (Figure 3A). To delve into the relationship between neuronal
211 activities and ripples, we aligned traces of ripple power with population synchrony and ripples. In a
212 recording session where 64 synchronous ensembles and 12 ripples were detected during
213 immobility, the LFP power at ripple frequency (120-240 Hz) exhibited no discernable peaks within
214 any of the synchronous events (Figure 3B, left upper and middle panels). Nevertheless, the same
215 LFP power displayed substantial peaks during every ripple event (Figure 3B, right upper and middle
216 panels). A striking contrast between synchronous events and ripples was also evident when spiking
217 probabilities during these events were examined. During population synchrony, the mean spiking
218 probability averaged across all cells was high, while the spiking probability was almost zero during
219 ripple events (Figure 3B lower panel). In the three sessions where ripples were identified, we
220 calculated the percentages of ripple events coinciding with synchronous ensembles and vice versa.
221 Remarkably, there was no co-occurrence of ripples and synchronous ensembles (Figure 3C).
222 Furthermore, we quantified ripple-modulated spiking by calculating the ratio of the difference in
223 mean firing rates during in-ripple and out-ripple periods to the sum of the mean firing rates during
224 both periods. Indexes of most cells were negative, and a striking 85% of cells displayed ripple
225 modulation indexes of -1, indicating complete suppression of their spiking activities during ripples
226 (Figure 3D). Taken together, during novel exploration, synchronous ensembles involved many
227 neurons with millisecond-synchronized spikes and occurred outside the time frames of ripples.

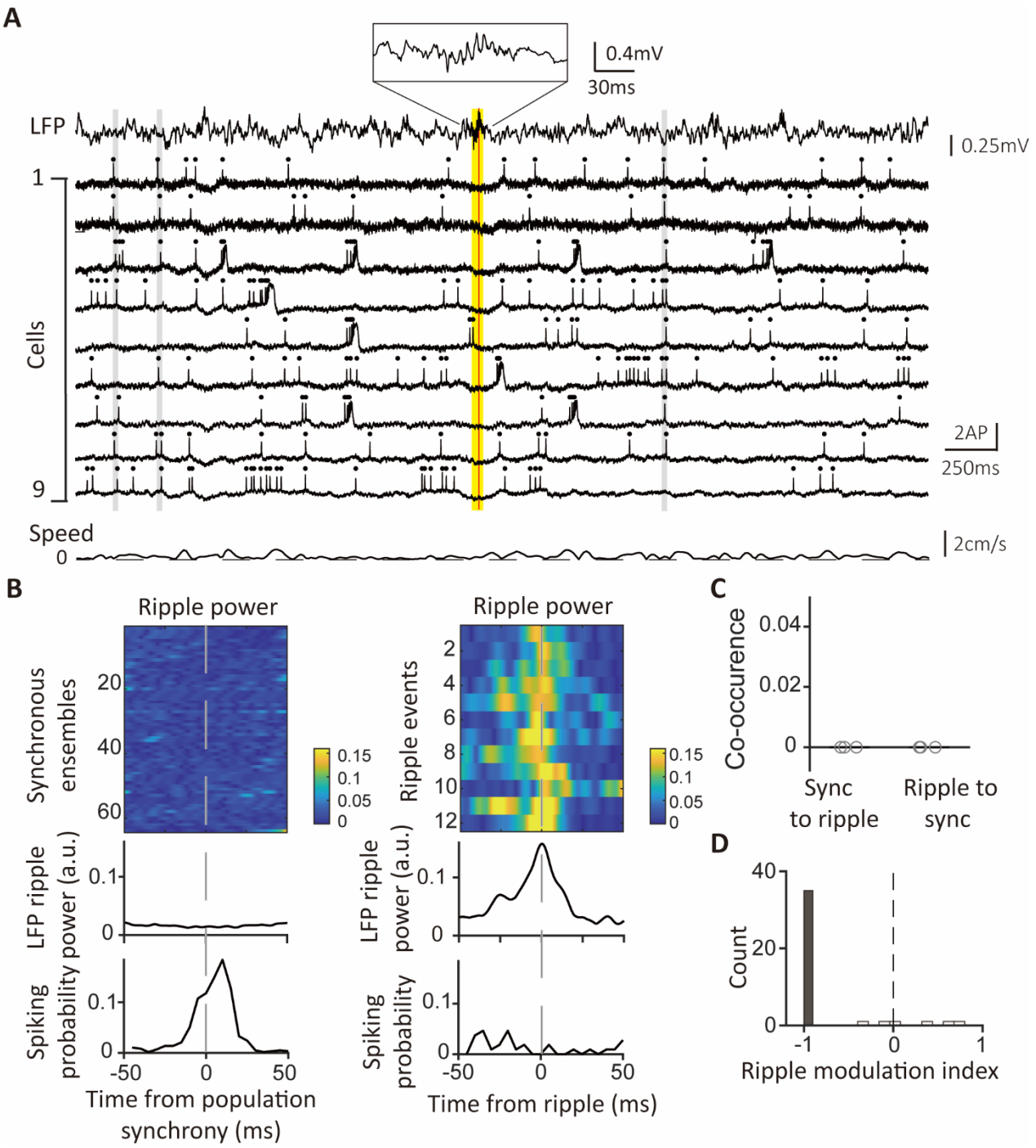

Figure 3. Synchronous ensembles occur outside ripple episodes.

(A) Example traces with ripples and synchronous ensembles. Top: simultaneously recorded LFP displaying an episode of ripple oscillation. A red vertical line indicates the timing of the peak ripple power in the LFP trace. A yellow vertical bar marks the duration of the ripple episode. Inset at the top: a magnified view of the ripple oscillation. Middle: fluorescence traces of 9 CA1PCs. Gray

235 vertical bars mark the timings of the synchronous ensembles on all traces. Bottom: animals' speed
236 recorded simultaneously with voltage imaging.
237 **(B)** LFP ripple power and spiking probability aligned to synchrony ensembles and ripple events.
238 Upper panel: color-coded LFP power at ripple frequency (120-240Hz) aligned to the timings of 64
239 synchronous ensembles (left) and 12 ripple events (right). Middle panel: Average LFP power of
240 ripple frequency aligned to the timings of the synchronous ensembles (left) and the ripple events
241 (right). Lower panel: Average spike counts of all cells aligned to the timings of the synchronous
242 ensembles (left) and ripple events (right).
243 **(C)** Percentages of co-occurrences between population synchrony and ripples. The co-occurrences
244 in the "sync to ripples" group represent the percentages of ripple episodes co-occurring with
245 synchronous ensembles in the same episodes. The co-occurrences in the "ripples to sync" group
246 indicate the percentages of synchronous ensembles co-occurring with ripple episodes. Each gray
247 circle represents an individual session.
248 **(D)** Distribution of the ripple modulation indexes (*n*=41 cells). Gray bar: modulation indexes with
249 significant p values (*n*=35 cells); white bars: modulation indexes without significance (*n*=6 cells).
250
251 It was puzzling that these CA1PCs exhibited robust spiking activities outside of ripples yet generated
252 few spikes during ripples. To further investigate neuronal activities during ripples, we established a
253 recording condition that allowed us to capture more ripple episodes. Specifically, we immobilized
254 mice in a tube to promote behaviors favoring ripple generation. The mice were habituated to head
255 fixation in a tube in a room distinct from the one where imaging experiments were conducted. On
256 the imaging day, the mice were introduced to the recording room and head-fixed under the
257 microscope for the first time.
258
259 CA1PCs were labeled *in utero* on embryonic day (E) 14.5 (*n*=56 cells from 3 sessions in 3 mice) and
260 E17.5 (*n*=55 cells from 3 sessions in 3 mice) and imaged in adult brains. Both neuronal populations

261 exhibited prominent peaks in their grand average CCGs and significantly higher synchronous event
262 rates compared to jittered data (Figure 3-figure supplement 2A, B). Approximately 40% of the
263 recorded neurons participated in synchronous ensembles, indicating robust synchronous activity
264 involving a substantial proportion of the recorded cells (Figure 3-figure supplement 2C).
265
266 In total, 1052 synchronous ensembles and 174 ripple episodes were detected across these imaging
267 sessions. Consistent with findings from walking animals, few synchronous ensembles occurred
268 during ripples when animals were immobilized in a tube (Figure 3-figure supplement 3A, B).
269 Moreover, no distinguishable ripple oscillations were observed in synchronous events, and the
270 average firing rates during ripple episodes were near zero (Figure 3-figure supplement 3C, D). At the
271 single-cell level, 90% of neurons showed significant negative spiking modulation during ripples, with
272 ripple modulation indexes close to -1, indicating strong suppression of spiking (Figure 4Ai). This
273 suppression extended to subthreshold membrane potentials, as nearly all cells exhibited decreased
274 fluorescence during ripples compared to baseline (Figure 4Bi, Ci). These results demonstrate that
275 spiking activity and subthreshold membrane potentials are robustly suppressed during ripples.
276
277 Contextual novelty plays a critical role in shaping hippocampal neuronal activities[37-43]. To assess its
278 influence, we trained mice to become familiar with the imaging procedure and the recording
279 environment over five days and recorded CA1PC activities on the final day. Mean firing rates were
280 significantly reduced in the familiar group compared to the novel group (Familiar group: 1.1 to 5.2
281 Hz (25th-75th percentiles), median=2.3 Hz, n=66 cells, 6 sessions, 4 mice; Novel group: 1.7 to 6.0 Hz
282 (25th-75th percentiles), median=4.2 Hz, n=111 cells, 6 sessions, 6 mice, p=0.0083, Wilcoxon signed-
283 rank test). Additionally, 15% of the neurons in the familiar group exhibited significantly positive
284 spiking modulation by ripples, while fewer cells showed negative modulation compared to the novel
285 group (Figure 4A). During ripples, neurons in the novel group predominantly displayed
286 hyperpolarizing membrane voltage responses, whereas a subset of neurons in the familiar group

exhibited prominent depolarizing responses (Figure 4B). The mean fluorescence changes in the familiar group shifted toward depolarization compared to the novel group (Figure 4C). Finally, synchronous event frequencies were significantly lower in the familiar context, indicating weaker synchronous activities under familiar conditions (Figure 4D). These results demonstrate that hippocampal neuronal activities, particularly synchronous ensembles, are strongly influenced by contextual novelty.

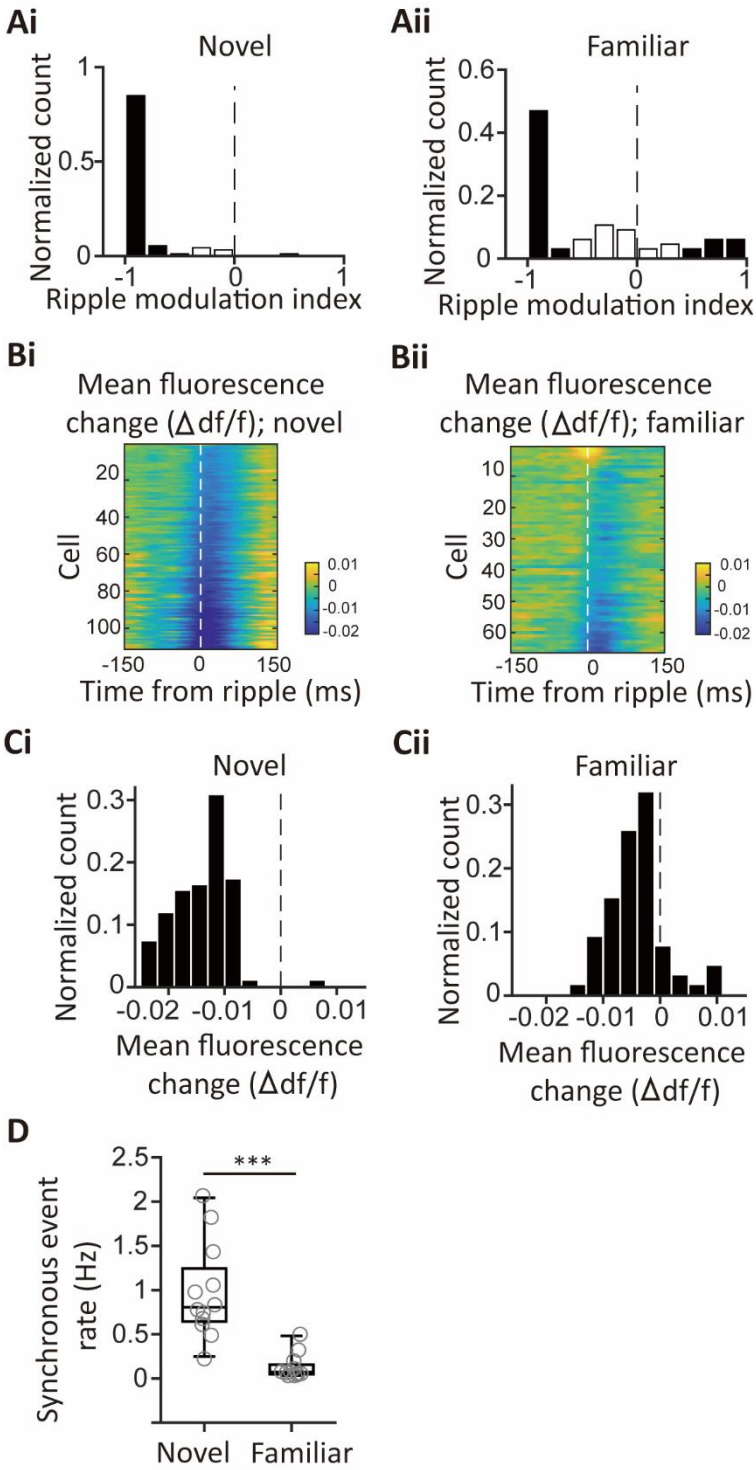

Figure 4. Comparison of ripple-associated neuronal activities and synchronous event rates between novel and familiar recording contexts.

(A) Histograms of ripple modulation indices for the novel (Ai) and familiar (Aii) recording contexts. Gray bars represent modulation indices with significant *p*-values, while white bars indicate non-significant modulation indices.

(B) Color-coded representations of mean fluorescence changes relative to baseline fluorescence for individual neurons, averaged across ripple events, in the novel (Bi) and familiar (Bii) recording contexts.

(C) Histograms of mean fluorescence changes within a ±10-ms window centered on the peak power of ripple events. Ci corresponds to the novel context, while Cii corresponds to the familiar context.

(D) Boxplots of synchronous event rates for the novel (Di) and familiar (Dii) recording contexts. Mean event rates were 0.98±0.16 Hz for the novel context and 0.13±0.04 Hz for the familiar context ($t(22)=5.20$, $p<0.001$, Student's *t*-test). ***$p<0.001$

Synchronous ensembles are associated with theta oscillations

To compare the network dynamics associated with synchronous ensembles during immobility and locomotion, we aligned LFP traces triggered to the timings of synchronous ensembles. The average LFP traces of a representative session showed prominent theta oscillations around the timings of both immobility and locomotion population synchrony (Figure 5A). Spectral analysis of the mean synchrony-triggered LFP traces during immobility and locomotion revealed theta frequency components of 4-12 Hz, with a slightly higher peak frequency in locomotion LFP compared to immobility LFP (Figure 5B). Furthermore, we computed LFP theta modulation and identified preferred phases of synchronous ensembles. In line with the previous result, synchronous ensembles displayed a high level of modulation by LFP theta oscillation (modulation strength: 0.61± 0.05 during immobility and 0.74±0.04 during locomotion, n=5 sessions). Although the preferred phases varied from session to session due to differences in recording sites along the proximal-distal axis of the hippocampus, the timings of individual ensembles were consistently locked to the preferred phase of each session (Figure 5C). These results establish a strong link between synchronous ensembles and LFP theta oscillation.

326 Subthreshold membrane voltage (subVm) is one of the critical parameters supporting the
327 generation of action potentials. To investigate the subthreshold signals underlying population
328 synchrony, we aligned subVm traces with the timings of synchronous ensembles and observed that
329 both immobility and locomotion synchrony rode on a subVm waveform oscillating at theta
330 frequency (Figure 5D). To elucidate further the relationship between subVm theta oscillation and
331 spikes involved in population synchrony, we calculated the subVm theta modulation and preferred
332 phases of spikes. Spikes participating in both immobility and locomotion synchrony were strongly
333 coupled to the subVm theta oscillation of neurons, with the mean preferred phase being in the
334 latter half of the rising phase closer to subVm theta peaks (Figure 5E). Conversely, spikes not
335 participating in synchronous ensembles had weaker modulation strength compared to spikes
336 involved in synchrony (Figure 5-figure supplement 1A, B). Furthermore, the membrane voltages
337 triggered by these two categories of spikes showed a significant difference in the hyperpolarization
338 phase of the theta oscillation. Synchronous spikes were situated within cycles of theta oscillations
339 featuring more hyperpolarized troughs than spikes outside synchronous ensembles (Figure 5-figure
340 supplement 1C, D). Thus, compared to spikes not participating in synchronous ensembles,
341 synchronous spikes showed a more robust modulation by theta oscillation of membrane voltage
342 during immobility and locomotion in the context of novel exploration.
343
344 Notably, phase locking of spikes to their subVm theta oscillation and the synchronous spikes among
345 many neurons suggest that subVms of different neurons would be correlated at the theta frequency.
346 To explore the possibility, we divided the 180-second subVm traces into 1-second segments with
347 50% overlap and calculated the cross-correlation and magnitude-squared coherence function for
348 each pair of cell segments. Segments were sorted into the immobility or locomotion group based on
349 the animals' speed during each segment (kept below 1 cm/s for immobility and above 3 cm/s for
350 locomotion for more than 90% of the time). In total, we analyzed 511 cell pairs from 5 sessions.
351 Indeed, the cross-correlation of subVm between cell pairs revealed a high correlation at zero lag and

352 periodic modulation of the correlation at theta frequency (Figure 5F). Furthermore, the subVm
353 theta coherences were increased in both groups (immobility: 0.50, locomotion: 0.40, median, *n*=511
354 pairs) and were negatively correlated with soma distances (immobility: -0.46, locomotion: -0.48,
355 *n*=511 pairs, Figure 5G). Taken together, during novel exploration, CA1PCs generate synchronous
356 activity associated with theta oscillation and exhibit correlated and theta-coherent subVms.
357
358 Correlated intracellular theta and theta-phase locking of the synchronous ensembles raise the
359 question of whether population synchrony among CA1PCs extends beyond synchrony derived from
360 these effects. To address this, we analyzed population synchrony after randomizing the theta cycles
361 during which neurons spiked, while keeping their theta phases unchanged. Supplementary Figure 4
362 illustrates a significant reduction in synchronous event rates following theta cycle randomization.
363 The finding indicates spiking at specific theta cycles plays a major role in driving population
364 synchrony.
365
366 To further investigate synchronous ensembles across different datasets, we analyzed publicly
367 available hippocampal recordings 'hc-11' from the CRCNS repository[43,44], where rats navigated novel
368 mazes for water rewards (see Method). Using our algorithm, we identified a significant number of
369 synchronous ensembles during the first three minutes of novel navigation. On average, the rates of
370 synchronous events were 6.4-fold higher than those detected in jittered controls (mean event rate:
371 2.0 ± 0.3 Hz for the original data vs. 0.32 ± 0.03 Hz for jittered data, n = 8 sessions, p = 0.0078, W =
372 36, Wilcoxon signed-rank test; Supplementary Figure 5A). To assess whether ripple oscillations were
373 associated with these synchronous ensembles, we analyzed ripple event rates and their relationship
374 to population synchrony. During this period, ripple events were infrequent (mean ripple rate: 0.02 ±
375 0.01, n = 8 sessions), and ripple power peaked during ripple episodes but remained low at the
376 timings of population synchrony (Supplementary Figure 5B). Nevertheless, LFP traces aligned to
377 population synchrony revealed prominent theta oscillations (Supplementary Figure 5C).

Synchronous ensembles were modulated by LFP theta oscillation (modulation strength: 0.30 ± 0.04, n = 8 sessions, $p < 0.001$), and the timings of individual ensembles were consistently locked to the preferred phase of each session, suggesting a functional coupling of synchronous ensembles to theta oscillations important for information processing (Supplementary Figure 5D).

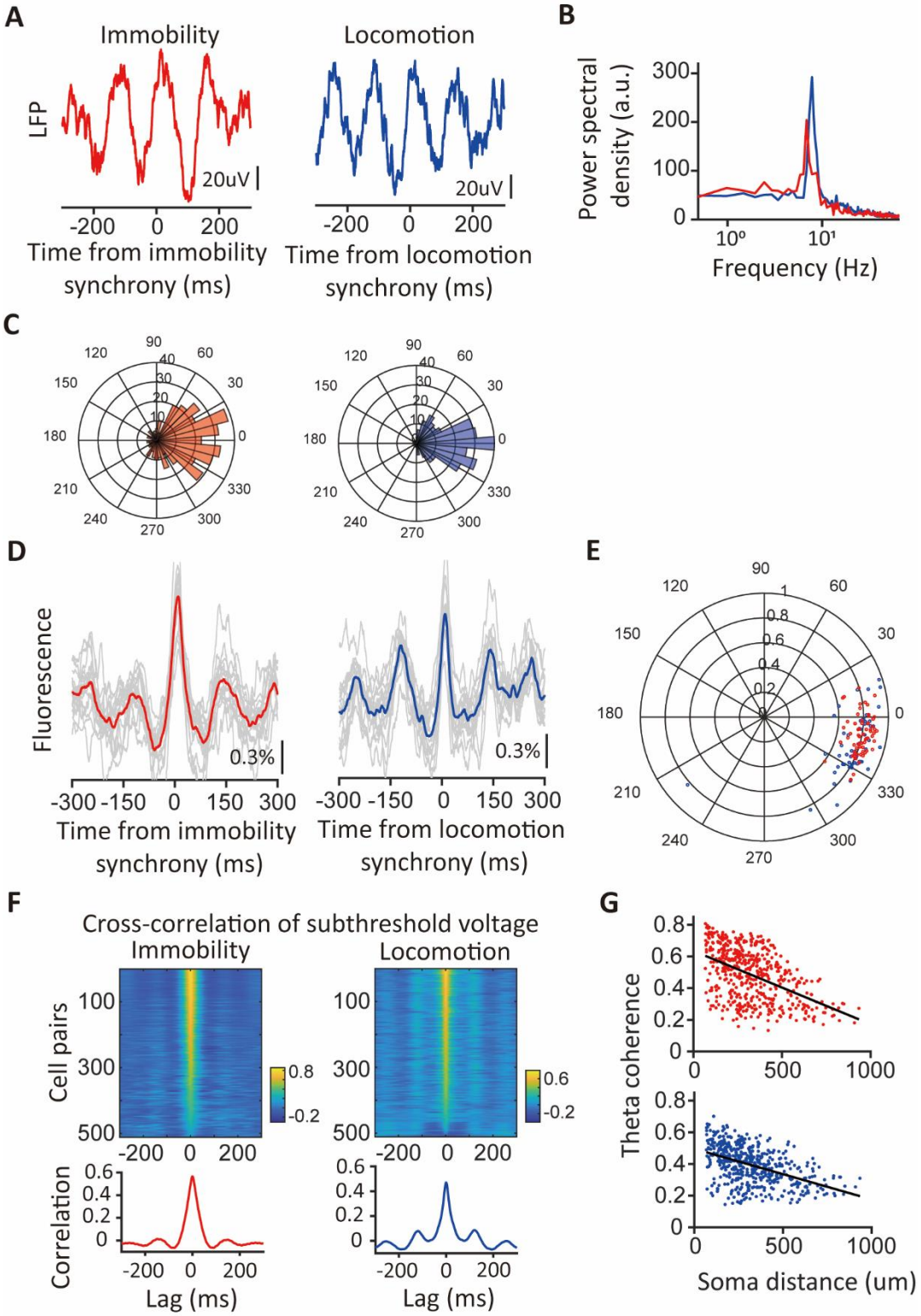

Figure 5. Theta oscillations in the LFP and subthreshold membrane potential were linked to population synchrony.

(A) LFP waveforms triggered by timings of synchronous ensembles. Red: triggered by timings of immobility synchrony; blue: triggered by timings of locomotion synchrony.

(B) Power spectral densities of the triggered LFP waveforms. Red: immobility; blue: locomotion.

(C) Distributions of the differences between LFP theta phases of individual synchronous ensembles and their preferred phases of the session. Note that most ensembles show minor differences within ±30 degrees. Red: immobility; blue: locomotion.

(D) Fluorescence traces triggered by timings of synchronous ensembles. Traces with spikes are excluded. Left panel: traces triggered by timings of immobility synchrony. Right panel: traces triggered by timings of locomotion synchrony. Thin gray lines: mean triggered fluorescence traces averaged across triggers for representative cells. Thick red and blue lines: mean triggered fluorescence traces averaged across cells.

(E) Polar plot illustrating theta modulation of spikes participating in the immobility synchrony (red dots) and of spikes participating in the locomotion synchrony (blue dots). The angle of the dots indicates the preferred phase, and the distance from the center of the circle represents the modulation strength. Each dot represents the averages from a neuron.

(F) Pairwise cross-correlation of the subthreshold membrane voltages (subVm). Top: color-coded cross-correlation of subVm between cell pairs during immobility and locomotion periods. Bottom: averaged cross-correlation over all cell pairs for immobility (red) and locomotion (blue) subVm. Both show a central peak at zero lag flanked by theta oscillation.

(G) Scatter plots of theta coherence against soma distances of immobility subVm (red) and locomotion subVm (blue) between cell pairs.

407 **Synchrony between place cells with distinct place tunings**

408 When animals explore a novel maze, spatially tuned spiking activity can form within a few
409 minutes[45,46]. However, how synchronous ensembles organize their spatially tuned activities during
410 novel exploration remains to be determined. Synchronous ensembles, generating spikes
411 coincidently in short intervals, might display correlated spiking at longer time windows that match
412 behavioral timescales of exploration, potentially leading to shared place responses. On the other
413 hand, CA1PCs are interconnected through inhibitory interneurons[47-49]. Modulation of activities in
414 inhibitory interneurons by some place cells may influence the activities of other place cells,
415 resulting in divergent spatial tunings[45,50,51].

416

417 To compare the spatial tunings of synchronous cell pairs, we first calculated the spatial tuning
418 curves of individual neurons by computing the mean firing rates in every spatial bin. On average,
419 40% of cells displayed selective spatial tunings of their spiking activities and were qualified as place
420 cells[52] (Figure 6A). Among place cell pairs, some showed similar spatial tunings, while others did not
421 (Figure 6B). For instance, in an illustrative session depicted in Figure 6B, the seventh and eighth
422 place cells had highly similar spatial tunings with a correlation coefficient as high as 0.7. In contrast,
423 the fifth and tenth place cells exhibited vastly different spatial tunings with a correlation coefficient
424 as low as -0.5.

425

426 We further explored the relationship between the similarity of spatial tunings and synchronization
427 strength among pairs of place cells. We measured synchronization strength as the peak of the CCG
428 normalized by the averaged jittered spike count within the same bin as the CCG peak. We
429 segregated spikes based on these behavioral states to accommodate differences between
430 locomotion and immobility and calculated the corresponding CCG and synchronization strength.

431

432 During locomotion, we observed a robust negative correlation between synchronization strength

433 and the similarity of spatial tunings among cell pairs. In other words, cell pairs with more precisely
434 co-active spikes during locomotion exhibited more distinct place-tuning profiles (Figure 6C, D). This
435 anti-correlation between synchronization strength and place tunings indicates coordination
436 between place cells' temporal and spatial coding. On the other hand, synchronization strength
437 during immobility showed little correlation with the similarity of spatial tunings among place cell
438 pairs, suggesting that correlated activities at the millisecond timescale do not extend to slow,
439 behavioral-relevant timescales (Figure 6-figure supplement 1). Thus, place cells with distinct place
440 fields are linked by synchronous activity during novel locomotion.
441

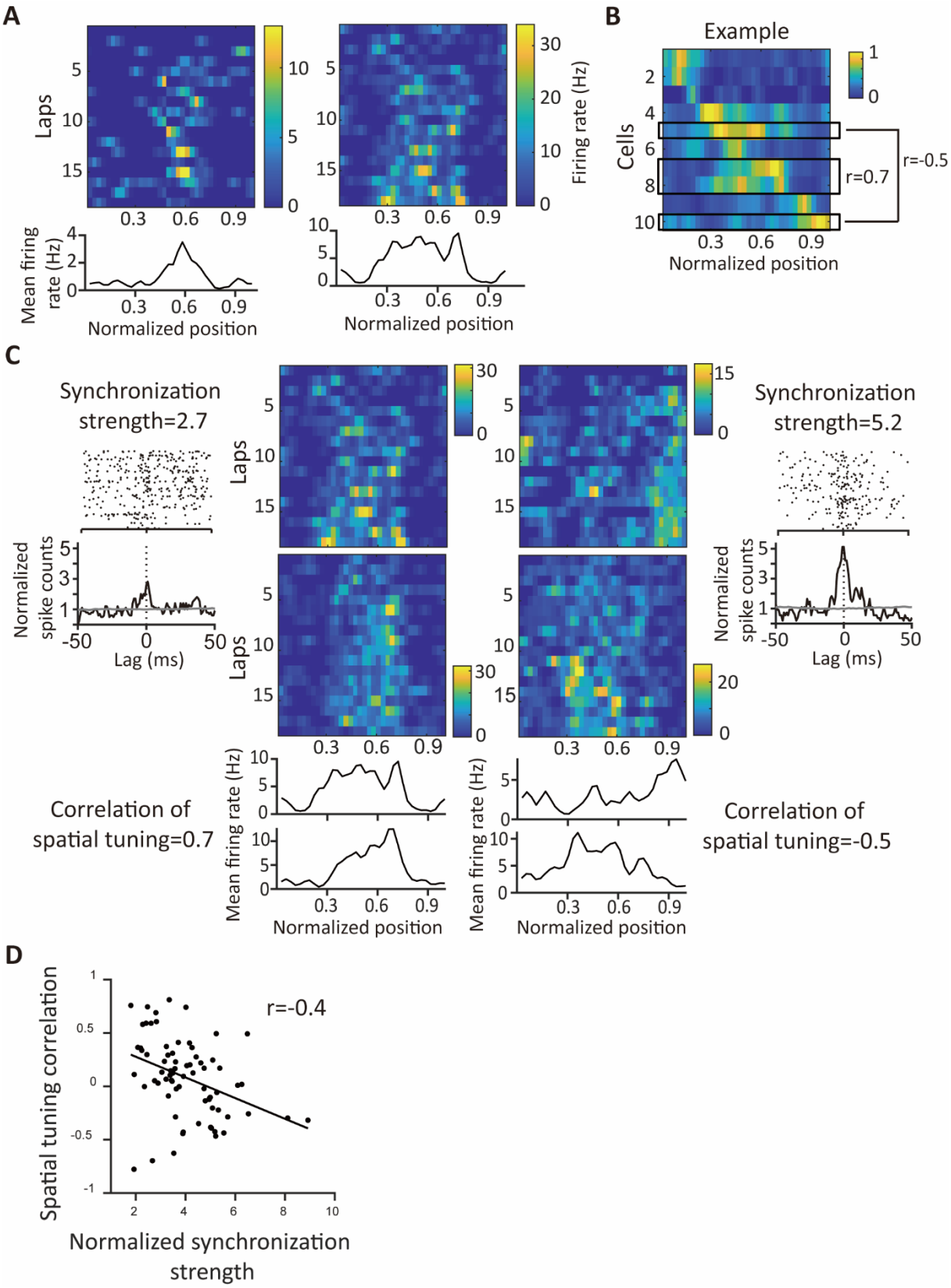

Figure 6. Negative correlation between spatial tuning similarity and synchronization strength during novel exploration.

445 **(A)** Spatially binned rate maps of place cells. High firing rates are indicated in yellow, and low firing
446 rates are noted in blue. Bottom: the mean firing rates along spatial bins averaged across laps.
447 **(B)** Spatial tunings of 10 place cells from an example session. Cells are sorted based on the locations
448 of their peak firing rates.
449 **(C)** Two example pairs of neurons with cross correlograms during locomotion and spatially binned
450 firing rate maps.
451 **(D)** A scatter plot of correlation coefficients of spatial tunings against normalized synchronization
452 strengths for place cell pairs. Each dot represents a pair of place cells. Synchronization strengths are
453 negatively correlated with similarities of spatial tunings (Spearman correlation coefficient=-0.4,
454 $p<0.001$, $n=73$ pairs).
455
456

457 ## Discussion

458 Our findings reveal the presence of synchronous ensembles comprising a substantial number of
459 CA1PCs during both locomotion and immobility in a novel environment. These ensembles
460 concurrently engage neurons representing diverse aspects of the environment and are rarely
461 observed during ripple events. Instead, they closely align with LFP and intracellular theta
462 oscillations. Our data demonstrate theta-associated synchronous ensembles during spatial memory
463 acquisition, coordinating numerous CA1 place cells that transmit information about different
464 segments of the environment.
465
466 The correlation between observed population synchrony and theta oscillations is intriguing. Theta
467 oscillations are typically associated with the sequential activation of neurons over time, resulting in
468 reduced neuronal synchrony[22]. However, theta oscillations come in different types, each
469 characterized by distinct pharmacological properties and behavioral correlates[53-55]. For example,
470 type 1 theta, or translational theta, occurs during voluntary movements and is sensitive to N-

methyl-D-aspartate receptor (NMDAR) blockers. On the other hand, type 2 theta, or attentional theta, is slightly slower and is blocked by muscarinic receptor antagonists, emerging during states of arousal or attention, such as when entering a new environment[56-58]. Consistent with these distinctions, the peak of the power spectrum density shows a distinctively slower theta frequency during immobility compared to locomotion (Figure 5B).

During theta oscillations, cholinergic neurons in the medial septum excite downstream CA1PCs, leading to increased firing rates and membrane potentials[59-61]. Given the widespread influence of cholinergic inputs on numerous CA1PCs, theta-coupled cholinergic inputs may drive depolarization and firing across many CA1PCs. Additionally, they could enhance the likelihood of synchronicity. Furthermore, GABAergic neurons in the medial septum, activated during theta oscillations, could activate interneurons in the CA1 region[55,62,63]. These CA1 interneurons, in turn, have the capability to entrain the activities of pyramidal neurons at both sub- and suprathreshold levels, thereby promoting synchronization among pyramidal neurons[64,65]. In summary, cholinergic and GABAergic neuron activation during theta waves may contribute to the excitation of CA1PCs and the consequent increase in their synchronicity.

Theta oscillations have long been implicated in memory acquisition. Specifically, theta power correlates positively with learning performance[66-68]. Perturbing generation of theta waves leads to impairment in memory acquisition[69-73], while electrical stimulation restoring theta rhythms rescues learning performance[74,75]. Furthermore, increased spike-theta coherence correlates with better memory, and stimulations that boost theta phase-locking of spikes enhance memory[76-78]. Despite abundant evidence supporting a link between theta oscillations and memory, the precise network mechanism by which theta oscillations support memory acquisition remains unclear. Theta oscillations are hypothesized to link spatially distributed neurons into functional ensembles to support memory acquisition[13]. The identified synchronous ensembles support the hypothesis,

497 providing a network substrate that links theta rhythms to the initial stage of memory acquisition.
498
499 Recent studies have demonstrated elevated coactivity of hippocampal principal cells during theta-
500 associated dentate spikes, events that are temporally coupled to theta oscillations and distinct from
501 sharp-wave ripples[79-81]. These findings highlight a network state characterized by rich synchronous
502 ensembles associated with theta, but not ripple, oscillations-a pattern consistent with our results.
503 Our analyses of publicly available data further support these observations, revealing theta-
504 associated population synchrony in a different dataset (Supplementary Figure 5). These results
505 suggest that hippocampal neurons achieve synchrony through network mechanisms distinct from
506 ripple-related events, reinforcing the hypothesis that this phenomenon is generalizable across
507 experimental conditions and behavioral contexts.
508
509 Previous studies have reported that a small percentage of CA1PCs generate spikes during ripple
510 episodes[8,14,17]. These measurements are typically conducted in familiar environments. In contrast,
511 when animals are introduced to a novel environment, ripple-associated spiking activities are
512 strongly suppressed, and CA1PCs exhibit prominent hyperpolarizing responses in their membrane
513 potentials (Figure 3, 4Ai-Ci, and Figure 3-figure supplement 3). Interestingly, after familiarization
514 training, a larger proportion of CA1PCs display positive ripple modulation of spiking activities and
515 depolarizing responses associated with ripples (Figure 4Aii-Cii). Consistent with the observation of
516 ripple-associated spiking activity in familiar environments, our study underscores the influence of
517 contextual novelty on hippocampal dynamics. Specifically, brain states associated with novelty may
518 modulate the activity of neurons upstream of CA1PCs, driving their membrane potentials toward
519 hyperpolarization during ripples. While the reduced correlation between ripples and spikes in novel
520 environments may initially appear counterintuitive, this unique neuronal activity pattern likely
521 reflects adaptive changes in hippocampal circuits related to the animals' behavioral states, such as
522 heightened vigilance in novel environments.

523

524 Although CA1PCs are known to exhibit weaker recurrent connectivity than that of CA3 pyramidal
525 neurons, CA1PCs did communicate through monosynaptic connections[82]. These connections can be
526 dynamically adjusted by the spike-timing-dependent plasticity mechanism[83-85], and therefore could
527 be affected by the transient population synchrony. In addition, CA1PCs are known to communicate
528 through inhibitory interneurons. Multiple pyramidal neurons converge onto a single interneuron,
529 and individual connections are often weak and unreliable[48,86,87]. This connectivity scheme requires
530 multiple pyramidal neurons spiking synchronously within the time window of synaptic integration to
531 effectively activate postsynaptic neurons[48]. Furthermore, population synchrony among CA1PCs may
532 propagate to downstream areas, synchronizing neurons outside the hippocampus. With their large
533 ensemble sizes, these synchronous ensembles may synergistically convey relevant information or
534 reorganize the connectivity of the neuronal networks.

535

536 Prior studies in sensory systems have commonly revealed that neurons with synchronous activities
537 typically share similar sensory responses[88,89]. However, the synchronous ensembles we have
538 identified often encompass neurons with distinct preferences for place fields. Pairwise synchrony
539 demonstrates a negative correlation with place field overlap (Figure 6). These findings indicate that
540 synchrony does not necessarily imply similar tunings between neurons. Furthermore, these
541 synchronous ensembles involve place cells encoding different spatial information. Recognizing the
542 crucial role of neuronal synchrony in binding distributed neurons in the brain[3,5], population
543 synchrony may serve as a mechanism to integrate diverse features of the same environment into a
544 cohesive mental map.

545

546 # Methods

547 **Animal**

548 Time-pregnant wild-type C57BL/6J female mice underwent in utero virus injection of CamkII-cre
549 virus (105558-AAV1, Addgene) into the left side of the lateral ventricles. The resulting offspring
550 were raised in a breeding room under controlled temperature and humidity conditions and a 12-
551 hour light/dark cycle (lights on from 7:00 to 19:00). The mice used in the experiments were
552 between 12 and 18 weeks old at the time of the recordings. All surgical procedures, behavioral
553 training, and recording protocols were approved by the NYCU Institutional Animal Care and Use
554 Committee.

555

556 **In-utero virus injection**

557 Time-pregnant mice on embryonic day 14.5 or 17.5 were anesthetized with isoflurane (induction:4-
558 5%; maintenance:1-3%) before surgery. The animals were placed on a heating pad in a supine
559 position to maintain body temperature. Aseptic procedures were implemented to maintain sterile
560 conditions during the surgery. Uterine horns were exposed one at a time using spoons and fingers.
561 Warm and sterile phosphate-buffered saline (PBS) was used to rinse the uterus to prevent it from
562 drying out. Micropipettes loaded with CamkII-cre virus solution were used to inject 0.2 μL of virus
563 suspension into the left side of the lateral ventricle of each embryo. The injection resulted in Cre
564 expression among neurons born on the day of injection, with earlier injection labeling neurons
565 located on the deeper side of the cell layer. The uterine horn was then gently returned to the
566 abdominal cavity. The exact process was repeated to the other uterine horn. After the surgery,
567 ketorolac (6mg/kg) and cefazolin (1g/kg) were administered for two days to minimize pain and
568 inflammation.

569

570 **Cranial window and cannula implantation**

571 The offspring of the mice that had undergone in-utero injection were subjected to chronic
572 hippocampal window surgery when they were between 2 and 4 months old. The animals were
573 initially anesthetized using isoflurane (induction:4-5%; maintenance:1-3%). Topical anesthesia was
574 applied by administering 0.5% lidocaine to the wound margins. After achieving deep anesthesia, an
575 incision was made in the skin, and a circular section of the skull was removed, centered 2 mm
576 caudal and 1.8 mm left to the bregma. Using 30-gauge needles and forceps, the dura was removed
577 from the exposed area, and cortical tissue within the craniotomy was aspirated. A serial dilution
578 experiment was conducted to determine an optimal titer of the virus carrying Voltron2 genes,
579 minimizing cell toxicity, for use in this and in previous imaging experiments[29]. A fine injection
580 pipette (tip diameter 10-60 um) was used to inject AAV2/1-CAG-flex-Voltron2-ST (2.7×10^{12} GC/ml, a
581 generous gift from Dr. Eric Schreiter and the GENIE team at HHMI Janelia Research Campus) into the
582 exposed regions at a depth of 200 μm (up to six injection sites and 100-200 nL of viral
583 suspension). An optical chamber was constructed by placing a cannula with a cover slip attached at
584 the bottom over the craniotomy and sealing it with dental acrylic or C&B Metabond (Sun Medical).
585 A custom-built titanium frame was then cemented to the animal's head using dental acrylic or C&B
586 Metabond. Mice received ketorolac (6mg/kg) and cefazolin (1g/kg) for two days following surgery to
587 minimize pain and inflammation.
588
589 **Behavioral training**
590 After at least two weeks of recovery from the window surgery, the mice underwent behavioral
591 training to ensure they were calm and attentive in the test environment. For mice subjected to
592 imaging experiments where they explored an air-lifted plastic track, the initial training phase
593 involved acclimating the mice to head fixation and treadmill running, which took place over 3-5 days
594 in a separate room distinct from the recording setup. Following this training, the imaging
595 experiments were conducted. On the day designated for imaging, the mice were introduced to the
596 recording room for the first time just before the imaging session. During the imaging experiments,

597 the mice were securely held in a head-fixed position beneath the microscope and on an air-lifted
598 plastic track that rested on an air table (AirLift, Neurotar; Figure 1A). The track was adorned with
599 various shapes of signs to help the mice navigate the track. Subdued blue lighting was provided to
600 illuminate the track. Before the initiation of imaging, the mice were confined in a corner of the track
601 using gates. Subsequently, the gates were opened upon the start of imaging, allowing the mice to
602 explore the new environment during their initial laps (Figure 1A Top view). The Mobile HomeCage
603 tracking system (Neurotar) was used to track the mice's position and speed. During the acquisition
604 of image frames, TTL pulses were sent by the high-speed camera to the Mobile HomeCage tracking
605 system to facilitate data alignment. Mice subjected to imaging experiments with head fixation in a
606 tube were first trained in a separate room, distinct from the recording setup, for 1-2 days to
607 habituate them to the head fixation procedure. Following this training, the mice were introduced to
608 the recording room for the first time immediately before the imaging session. During imaging, the
609 mice were securely positioned in a head-fixation setup within an acrylic tube and remained
610 stationary. To further familiarize the mice with the recording context, the imaging procedure was
611 repeated for 4 days without injecting the JF-HaloTag ligand. On the fifth day, the JF-HaloTag ligand
612 was injected prior to imaging, and voltage imaging was performed following the same procedure as
613 in the previous sessions.
614
615 **Voltage imaging**
616 JF_{552}-HaloTag ligand[90] (a generous gift from Dr. Luke Lavis) was first dissolved in DMSO (20 μl,
617 Sigma) and then diluted in Pluronic™ F-127 (20 μl, P3000MP, Invitrogen) and PBS to achieve a
618 final concentration of 0.83 mM of JF_{552}-HaloTag ligand. The solution was then injected intravenously
619 through the retro-orbital sinus. Imaging sessions were initiated 3 hours after the injection of the
620 JF_{552}-HaloTag ligand. Fluorescence sensors were excited using a 532-nm laser (Opus 532, Laser
621 Quantum) with an excitation filter (FF02-520-28, Semrock), and the emitted light was separated
622 from the excitation light using a dichroic mirror (540lpxr Chroma) and passed through an emission

filter (FF01-596183 Semrock). A 16X, 0.8 NA objective (Nikon) was used to collect the emission light which was then imaged on a CMOS camera (DaVinci-1K, RedShirt) with a 50-mm camera lens (Nikkor 50mm f1.2, Nikon) as the tube lens. Images were acquired using Turbo-SM64 (Sci-Measure) at 2kHz with a resolution of 190 x 160 pixels, corresponding to a field of view of 1.4 x 1.2 mm. The number of frames in an image session was set at 360,000, corresponding to a duration of 180 seconds per session. Imaging depths ranged between 70 and 170 μm from the window surface, where the CA1 pyramidal neurons were located. Time-lapse images were collected, and image stacks of the same field of view along the z-axis were acquired. The image stacks consisted of 100 plans separated by two μm, covering the depth from the window surface to 200 um from the surface.

LFP recording

The LFP signal from the contralateral CA1 region of the hippocampus was simultaneously recorded during voltage imaging. To implant the LFP electrode, a small craniotomy was performed at the dorsal CA1 coordinate (2mm caudal and 1.8 mm right to the bregma). A tungsten electrode (#100211, 38 μm in diameter, polyimide insulated, California Fine Wire) was inserted into the dorsal CA1 region, and the wire and pins were cemented in place with dental acrylic. The electrical signal was amplified and filtered (1-1kHz) using a DAM80 amplifier (Word Precision Instruments). The amplified signal was acquired by an I/O device (National Instruments USB-6341) and recorded using WaveSurfer (Adam Taylor, HHMI Janelia Research Campus) at 10 kHz during implantation and TurboSM64 (RedShirt) at 8 kHz during imaging.

Imaging somata and dendrites *in vivo* using a two-photon microscope

Immediately after voltage imaging, Voltron-labeled neurons were examined *in vivo* under a two-photon microscope to assess the integrity of their membranes and dendrites. Images were acquired using a two-photon scanning microscope equipped with a femtosecond-pulsed laser (Chameleon,

649 Coherent) and a resonant scanner controlled by ScanImage 4.2 software[91] (http://scanimage.org). A
650 16x water-immersion objective (Nikon, 0.8 NA, 3 mm working distance) was used for imaging. Z-
651 stacks of images (512 x 512 pixels, 600 μm x 600 μm) were collected with excitation light at 800
652 nm. The emission light was separated from the excitation light using a primary dichroic mirror
653 (FF735-Di02-25x36, Semrock), followed by a secondary dichroic mirror (565dclp, Chroma) and an
654 emission filter (FF01-609/57-30-D, Semrock). Each image stack consisted of 100 planes, separated
655 by 2 μm, covering depths from the window surface to 200 um below the surface.
656
657 **Histological processing and quantification of soma depth**
658 Mice with Voltron2$_{552}$ labeling were anesthetized with intraperitoneal injections of ketamine (250
659 mg/kg) and xylazine (25 mg/kg) and transcardially perfused with 4% paraformaldehyde in
660 phosphate-buffered saline (PBS; 2 mL/g). The brains were post-fixed in 4% paraformaldehyde
661 overnight and then washed in PBS. Coronal brain sections, 50 μm thick, were prepared using a
662 VT1200 vibratome (Leica). Sections were mounted with Vectashield mounting medium containing
663 DAPI (VectorLabs) to visualize nuclei. The soma depth of Voltron-labeled cells was measured relative
664 to the border between the *stratum pyramidale* (SP) and the *stratum radiatum*. Depth values were
665 normalized to the thickness of the SP, with larger depth ratios indicating somata located deeper
666 along the radial axis.
667
668 **Voltage imaging preprocessing and spike detection**
669 Fluorescence intensities were corrected for brain movement using rigid registration. Regions of
670 interest (ROIs) were manually selected by grouping pixels that cover individual somata. Previous
671 studies have described and validated the procedure for imaging preprocessing and spike
672 detection[29,92,93]. In short, the fluorescence intensities of individual neurons were calculated by
673 averaging the fluorescence intensities of pixels from the same ROIs. Bleaching was corrected by
674 calculating the baseline fluorescence (F_0) at each time point as an average of the fluorescence

675 intensities within ±0.5 seconds around the time point. The dF/F was calculated as the F_0 minus the
676 fluorescence intensity of the same time point divided by F_0. Positive fluorescence transients were
677 detected to identify spikes from the high-passed dF/F traces created by subtracting the dF/F traces
678 from the median-filtered version with a 5-ms window. To simulate the noise of recordings, high-
679 passed dF/F traces were inverted, and the amplitudes of the transients detected from the inverted
680 traces were used to construct a noise distribution of the spike amplitudes. A threshold was set by
681 comparing the amplitudes of the detected transients with the noise distribution of the spike
682 amplitudes to minimize the sum of type I and type II errors. Spikes were first detected when
683 transients were larger than the threshold. Then, spike amplitudes smaller than half of the top 5%
684 spike amplitudes were excluded. The signal-to-noise ratio (SNR) was calculated for each neuron as a
685 ratio of the averaged spike amplitudes over the standard deviation of the high-passed dF/F traces,
686 excluding points 2 ms before and 4 ms after each detected spike to estimate the quality of the
687 recordings. The crosstalk between ROIs was routinely checked by examining the refractory periods
688 of neurons in auto-correlograms. Only neurons meeting the following criteria were included: (1)
689 SNR larger than 5, (2) full width at half maximum of the spike waveform longer than 0.8 ms, (3)
690 mean spike rates higher than 0.1 Hz, (4) distances between soma pairs at least 70 μm. Sessions
691 with at least nine neurons meeting the selection criteria were used for further analysis.
692
693 **Behavioral states of locomotion and immobility**
694 The periods of locomotion were defined as instances when the animals' speed exceeded 3 cm/s,
695 while periods of immobility were determined as instances when the animals' speed fell below 1
696 cm/s.
697
698 **Mean firing rates during locomotion and immobility**
699 To calculate the mean firing rates during locomotion, we counted the number of spikes during
700 locomotion periods and divided this number by the total duration of locomotion. Similarly, for mean

701 firing rates during immobility, we calculated the number of spikes that occurred during immobility
702 periods and divided this number by the total duration of immobility.
703
704 **Correlation between instantaneous firing rate and animal speed**
705 To estimate the instantaneous firing rates of individual neurons over time, we convolved their spike
706 trains with a Gaussian window of 250 ms. Subsequently, we calculated the Pearson correlation
707 coefficient between these instantaneous firing rates and the animal's speed for each neuron.
708
709 **Grand average cross-correlogram (CCG)**
710 Grand average CCGs were generated by constructing histograms of relative spike timings between
711 spikes of a reference cell and spikes of all other neurons in the same session as the target cell
712 population. Histograms were binned using 1-ms time bins. Spike counts were normalized by the
713 number of reference spikes times the number of all other neurons. An equal number of cells from
714 different sessions were randomly selected to form the shuffled target cell population to assess the
715 statistical significance of the CCG peaks. Subsequently, grand average CCGs were computed using
716 shuffled spike trains for comparison. Grand average CCGs were calculated using all spikes in the 180-
717 s recording periods, subsets of spikes during immobility periods (immobility grand average CCGs),
718 and subsets of spikes during locomotion periods (locomotion grand average CCGs).
719
720 **Detection of the population synchrony**
721 To assess population synchrony, we counted the number of spikes from all neurons within a sliding
722 window of 25 ms. To test the significance of the synchrony, we generated surrogate data by jittering
723 spike timings within a ±75-ms window 500 times. The means and standard deviations of each
724 sample point were calculated over the jitter population. Population synchrony was detected as
725 peaks when the spike count in the original data exceeded the mean plus four standard deviations of
726 the spike counts in the jittered data. Synchrony was also evaluated in modified spike trains,

727 including those where later spikes in bursts were removed and those where spike times were
728 shuffled across theta cycles while preserving phases. To estimate synchronous event rates, we
729 divided the entire 180-second recordings into halves and calculated the event rate in each of the 90-
730 s segments. Additionally, ensemble sizes were quantified by counting the percentage of neurons
731 participating in each synchronous event.
732 To detect population synchrony in a publicly available dataset, we analyzed the "hc-11" dataset
733 from CRCNS, which contains hippocampal recordings from rats running on novel mazes for water
734 rewards at designated locations[43,44]. Spikes recorded during the first three minutes of the novel-
735 maze running epochs were used to identify synchronous ensembles and generate jittered control
736 data. Spike counts for both the original and jittered data were calculated using a sliding 25-ms
737 window. The algorithm for testing the significance of synchrony was the same as described above.
738 Synchronous event rates were estimated using the entire 3-minute spike trains for both the original
739 and jittered data.
740
741 **Pairwise cross-correlogram (CCG) of neuronal pairs**
742 To compute the CCG, we first determined the time difference between spikes in the target and
743 reference neurons and then binned these values into 1-ms time bins. CCGs were only computed for
744 pairs with more than 100 counts within the CCG window of ±500 ms to ensure reliable correlation.
745 We defined the peak of the CCG as the local maxima within ±30 ms of lag. To assess the significance
746 of cross-correlations, we generated surrogate data by jittering the spike times of the target neuron
747 within a ±75 ms window. We computed the CCG peak for a thousand iterations and calculated p-
748 values by comparing the percentile of the peak in the null distribution of the jittered peak values.
749 The synchronization strength was estimated as the ratio between the original CCG peak and the
750 mean spike count of the same bin as the original CCG peak averaged across the jittered histograms.
751 For display purposes, the CCGs were smoothed using a 5-point moving average. CCGs were
752 calculated using all spikes in the 180-s recording periods, subsets of spikes during immobility

753 periods (immobility pairwise CCGs), and subsets of spikes during locomotion periods (locomotion
754 pairwise CCGs).
755
756 **LFP ripple analysis**
757 To detect ripples, we performed band-pass filtering of the LFP signal between 120 and 240 Hz,
758 followed by computing the envelope using the absolute values of the Hilbert transform, which was
759 then low-pass filtered at 20 Hz. The start and end times of ripples were identified by setting the
760 upper and lower thresholds at the mean plus 7 and 3.5 times the standard deviation of the
761 envelope, respectively. For a ripple event to be included, three conditions had to be met: (1) values
762 within the event were higher than the lower threshold, (2) at least one value exceeded the upper
763 threshold, and (3) the minimum duration of the event was 30 ms. The start and end times of a
764 ripple event were defined as the positive and negative crossings of the lower threshold,
765 respectively. We defined in-ripple periods as the time between the start and end of detected LFP
766 ripple events, while out-ripple periods were periods outside the in-ripple periods. The envelope
767 peak values of the detected ripple events were used as the time of ripple occurrence. These timings
768 were utilized as trigger timings to calculate averages triggered by ripples. Two co-occurrences were
769 quantified: the percentages of LFP ripple oscillations that occurred with synchronous ensembles
770 and the percentages of synchronous ensembles that occurred with LFP ripple oscillations. The same
771 ripple detection algorithm was applied to the hc-11 dataset. To account for artifacts in the
772 recordings, raw traces and power spectra of the detected events were plotted and inspected for
773 false positives.
774
775 **Ripple modulation index**
776 We utilized the ripple modulation index to assess changes in firing rates during ripples compared to
777 periods outside ripples. This index was computed as the ratio of the difference in mean firing rates
778 during in- and out-ripple periods to the sum of the mean firing rates during both periods.

Specifically, we first calculated the mean firing rate during in-ripple periods and the mean firing rate during out-ripple periods. Next, we subtracted the mean firing rate during out-ripple periods from the mean firing rate during in-ripple periods and divided the result by the sum of the mean firing rates during both periods. The resulting ripple modulation index indicates the magnitude and direction of the firing rate modulation during ripple compared to periods outside ripples. To assess the significance of the modulation index, we shuffled the spike timings and repeated the calculation a thousand times to generate a distribution of modulation indices from the shuffled data. The original modulation index was then compared to this distribution, and its significance was determined if it exceeded the 95% confidence level of the shuffled indices.

LFP traces triggered by population synchrony and analysis

The midpoints of the synchronous event intervals were utilized as triggers to align LFP traces from both our recordings and the hc-11 dataset. These traces were aligned within a $\pm$1-second window around the trigger time points. To calculate the spectral density functions of the aligned LFP traces, we performed a 16,384-point fast Fourier transform of the 2-second LFP traces. The power spectra were then estimated as the squared absolute values of the Fourier coefficients. Ripple power was calculated as the sum of the power distributed between 120 and 240 Hz. To calculate theta modulation strength and preferred angles of the synchronous ensembles, LFP was first filtered within the theta frequency range. Then, the phase $\varphi(t)$ and the instantaneous amplitude $A(t)$ of the filtered LFP were computed using the Hilbert transform. A vector $V_k = A(t_k)e^{i\varphi(t_k)}$ was assigned to each synchronous ensemble that occurred at time t_k. The modulation strength and the preferred phase angle were determined as the absolute value and the phase angle of the summed vector over all ensembles, respectively. Modulation strengths were normalized by the total length of all vectors.

Subthreshold membrane voltage (subVm)

To compute the subVm of individual neurons, we began by determining the difference between the raw dF/F signal and the high-pass version of dF/F. Next, we calculated the spike threshold for each cell by identifying the voltage value corresponding to the peak of the first derivative of the spike waveforms. Any fluorescence values in the slow dF/F time courses that surpassed the spike thresholds were linearly interpolated.

SubVm traces triggered by population synchrony

The midpoint of the time intervals, during which synchronous ensembles were detected, served as the reference points for aligning fluorescence traces within a $\pm$300 ms window around those reference points. To eliminate any interference from membrane potential fluctuations associated with spikes, we excluded aligned traces in cases where any spike occurred within the time intervals of the aligned traces.

SubVm theta modulation and phase preference of spikes occurred inside and outside the population synchrony events

The subVm was initially filtered within the theta frequency range. Subsequently, the phase $\varphi(t)$ and the instantaneous amplitude $A(t)$ of the filtered subVm were computed using the Hilbert transform. Spikes were categorized into four groups: those occurring during or outside immobility synchronous events and those occurring during or outside locomotion synchronous events. Within each category, a vector $V_k = A(t_k)e^{i\varphi(t_k)}$ was assigned to each spike that occurred at time t_k. The modulation strength and preferred phase angle were determined as the absolute value and phase angle, respectively, of the summed vector over all spikes within a category. To facilitate comparison between neurons, modulation strengths were normalized by the total length of all vectors. The significance of the modulation strength was tested by shuffling the spike timings and recalculating the modulation strength a thousand times to generate a distribution based on the shuffled spike timings. The original modulation strength was then compared to the distribution,

with significance determined if it exceeded the 95% confidence interval of the shuffled values. Significant modulation strengths were plotted and compared across groups.

Spike-triggered fluorescence traces

We extracted segments of fluorescence traces using a ±300 ms time window centered on the spike timings. To examine variations in fluorescence waveforms triggered by spikes within and outside synchronous events, we categorized the fluorescence traces based on whether the spikes occurred within or outside these events. Subsequently, we performed pairwise comparisons of the fluorescence values from the same neuron, concentrating on spikes occurring during corresponding behavioral states. Neurons with four or fewer triggering events in any of these categories were omitted from the analysis.

Cross-correlation and coherence analysis to the subVm traces

To calculate cross-correlation and theta coherence of subVm between pairs of neurons during locomotion and immobility, we initially divided the 180-second subVm traces into 1-second segments with a 50% overlap. These segments were then categorized into the locomotion group if the animal's speed remained above three cm/s for more than 90% of the time within that segment. Similarly, segments were sorted into the immobility group if the animal's speed remained below one cm/s for more than 90% of the time within that segment. Subsequently, we computed the cross-correlation and magnitude-squared coherence function of frequency for pairs of co-occurred segments belonging to a specific cell pair. Mean cross-correlations of individual cell pairs were averaged across segments that occurred in the same behavioral states (i.e., locomotion or immobility states). To estimate theta coherence, we averaged the values of the coherence function within the theta frequency range (4-12 Hz). Theta coherences from the same cell pair during the same behavioral state were pooled together, and the average was used as an estimate for the theta coherence of that cell pair during a particular behavioral state. Finally, Spearman correlation

857 coefficients were calculated between the mean theta coherences of cell pairs and their soma
858 distances.
859
860 **Spatial analysis**
861 We partitioned a 90-cm-long track into 36 spatial bins to analyze spatial tuning properties. For each
862 cell, the spatial tuning curve was computed by determining the mean firing rate, defined as the
863 number of spikes within the bin when the animal's speed exceeded three cm/s, divided by the total
864 dwell times using the same speed threshold. The peak firing rates were identified as the maximal
865 rate on the spatial tuning curve. Spatial selectivity was calculated as one minus the circular variance
866 of the spatial tuning curve. Neurons were classified as place cells when their spatial selectivity
867 exceeded 0.25, and peak firing rates exceeded 1 Hz. To assess the similarity of spatial tuning
868 between pairs of neurons, Spearman correlation coefficients were calculated for the spatial tuning
869 curves. To explore the relationship between levels of synchronization and spatial tuning similarity
870 among pairs of place cells, Spearman correlation coefficients were computed between
871 synchronization strengths of cell pairs and correlation coefficients of their spatial tuning curves.
872
873 **Data analysis and statistics**
874 Data analysis was performed using MATLAB (Mathworks, R2019b), and results were presented as
875 standard error of the mean unless otherwise specified. Boxplots were used to depict the median,
876 first quartile, and third quartile, with the middle line, the upper edge, and the lower edge of the
877 box, respectively. The whiskers of the boxplots represented the 5th and 95th percentiles of the
878 distribution.
879

1 Takeuchi, T., Duszkiewicz, A. J. & Morris, R. G. The synaptic plasticity and memory hypothesis: encoding, storage and persistence. *Philos Trans R Soc Lond B Biol Sci* **369**, 20130288 (2014). https://doi.org:10.1098/rstb.2013.0288

2 Moser, M. B., Rowland, D. C. & Moser, E. I. Place cells, grid cells, and memory. *Cold Spring Harb Perspect Biol* **7**, a021808 (2015). https://doi.org:10.1101/cshperspect.a021808

3 Axmacher, N., Mormann, F., Fernandez, G., Elger, C. E. & Fell, J. Memory formation by neuronal synchronization. *Brain Res Rev* **52**, 170-182 (2006). https://doi.org:10.1016/j.brainresrev.2006.01.007

4 Paulsen, O. & Sejnowski, T. J. Natural patterns of activity and long-term synaptic plasticity. *Curr Opin Neurobiol* **10**, 172-179 (2000). https://doi.org:10.1016/s0959-4388(00)00076-3

5 Wang, X. J. Neurophysiological and computational principles of cortical rhythms in cognition. *Physiol Rev* **90**, 1195-1268 (2010). https://doi.org:10.1152/physrev.00035.2008

6 Harris, K. D., Csicsvari, J., Hirase, H., Dragoi, G. & Buzsaki, G. Organization of cell assemblies in the hippocampus. *Nature* **424**, 552-556 (2003). https://doi.org:10.1038/nature01834

7 Squire, L. R. & Wixted, J. T. The cognitive neuroscience of human memory since H.M. *Annu Rev Neurosci* **34**, 259-288 (2011). https://doi.org:10.1146/annurev-neuro-061010-113720

8 Buzsaki, G. Hippocampal sharp wave-ripple: A cognitive biomarker for episodic memory and planning. *Hippocampus* **25**, 1073-1188 (2015). https://doi.org:10.1002/hipo.22488

9 Nadasdy, Z., Hirase, H., Czurko, A., Csicsvari, J. & Buzsaki, G. Replay and time compression of recurring spike sequences in the hippocampus. *J Neurosci* **19**, 9497-9507 (1999). https://doi.org:10.1523/JNEUROSCI.19-21-09497.1999

10 Cheng, S. & Frank, L. M. New experiences enhance coordinated neural activity in the hippocampus. *Neuron* **57**, 303-313 (2008). https://doi.org:10.1016/j.neuron.2007.11.035

11 Dragoi, G. & Tonegawa, S. Preplay of future place cell sequences by hippocampal cellular assemblies. *Nature* **469**, 397-401 (2011). https://doi.org:10.1038/nature09633

12 Liu, C., Todorova, R., Tang, W., Oliva, A. & Fernandez-Ruiz, A. Associative and predictive hippocampal codes support memory-guided behaviors. *Science* **382**, eadi8237 (2023). https://doi.org:10.1126/science.adi8237

13 Colgin, L. L. Rhythms of the hippocampal network. *Nat Rev Neurosci* **17**, 239-249 (2016). https://doi.org:10.1038/nrn.2016.21

14 Buzsaki, G. & Silva, F. L. High frequency oscillations in the intact brain. *Prog Neurobiol* **98**, 241-249 (2012). https://doi.org:10.1016/j.pneurobio.2012.02.004

15 Csicsvari, J., Hirase, H., Czurko, A. & Buzsaki, G. Reliability and state dependence of pyramidal cell-interneuron synapses in the hippocampus: an ensemble approach in the behaving rat. *Neuron* **21**, 179-189 (1998). https://doi.org:10.1016/s0896-6273(00)80525-5

16 Gillespie, A. K. *et al.* Hippocampal replay reflects specific past experiences rather than a plan for subsequent choice. *Neuron* **109**, 3149-3163 e3146 (2021). https://doi.org:10.1016/j.neuron.2021.07.029

17 Yagi, S., Igata, H., Ikegaya, Y. & Sasaki, T. Awake hippocampal synchronous events are incorporated into offline neuronal reactivation. *Cell Rep* **42**, 112871 (2023). https://doi.org:10.1016/j.celrep.2023.112871

18 El-Gaby, M. *et al.* An emergent neural coactivity code for dynamic memory. *Nat Neurosci* **24**, 694-704 (2021). https://doi.org:10.1038/s41593-021-00820-w

19 Skaggs, W. E., McNaughton, B. L., Wilson, M. A. & Barnes, C. A. Theta phase precession in hippocampal neuronal populations and the compression of temporal sequences. *Hippocampus* **6**, 149-172 (1996). https://doi.org:10.1002/(SICI)1098-1063(1996)6:2<149::AID-HIPO6>3.0.CO;2-K

20 Dragoi, G. & Buzsaki, G. Temporal encoding of place sequences by hippocampal cell assemblies. *Neuron* **50**, 145-157 (2006). https://doi.org:10.1016/j.neuron.2006.02.023

21 Foster, D. J. & Wilson, M. A. Hippocampal theta sequences. *Hippocampus* **17**, 1093-1099 (2007). https://doi.org:10.1002/hipo.20345

22 Mizuseki, K. & Buzsaki, G. Theta oscillations decrease spike synchrony in the hippocampus and entorhinal cortex. *Philos Trans R Soc Lond B Biol Sci* **369**, 20120530 (2014). https://doi.org:10.1098/rstb.2012.0530

23 O'Keefe, J. & Recce, M. L. Phase relationship between hippocampal place units and the EEG theta rhythm. *Hippocampus* **3**, 317-330 (1993). https://doi.org:10.1002/hipo.450030307

24 Lee, A. K. & Brecht, M. Elucidating Neuronal Mechanisms Using Intracellular Recordings during Behavior. *Trends Neurosci* **41**, 385-403 (2018). https://doi.org:10.1016/j.tins.2018.03.014

25 Petersen, C. C. H. Whole-Cell Recording of Neuronal Membrane Potential during Behavior. *Neuron* **95**, 1266-1281 (2017). https://doi.org:10.1016/j.neuron.2017.06.049

26 Giocomo, L. M., Zilli, E. A., Fransen, E. & Hasselmo, M. E. Temporal frequency of subthreshold oscillations scales with entorhinal grid cell field spacing. *Science* **315**, 1719-1722 (2007). https://doi.org:10.1126/science.1139207

27 Lampl, I., Reichova, I. & Ferster, D. Synchronous membrane potential fluctuations in neurons of the cat visual cortex. *Neuron* **22**, 361-374 (1999). https://doi.org:10.1016/s0896-6273(00)81096-x

28 Poulet, J. F. & Petersen, C. C. Internal brain state regulates membrane potential synchrony in barrel cortex of behaving mice. *Nature* **454**, 881-885 (2008). https://doi.org:10.1038/nature07150

29 Abdelfattah, A. S. *et al.* Sensitivity optimization of a rhodopsin-based fluorescent voltage indicator. *Neuron* (2023). https://doi.org:10.1016/j.neuron.2023.03.009

30 Angevine Jr, J. B. Time of neuron origin in the hippocampal region: an autoradiographic study in the mouse. *Experimental Neurology* (1965).

31 Bayer, S. A. Development of the hippocampal region in the rat. I. Neurogenesis examined with 3H-thymidine autoradiography. *J Comp Neurol* **190**, 87-114 (1980). https://doi.org:10.1002/cne.901900107

32 Cavalieri, D. *et al.* CA1 pyramidal cell diversity is rooted in the time of neurogenesis. *Elife* **10** (2021). https://doi.org:10.7554/eLife.69270

33 Cembrowski, M. S. *et al.* Spatial Gene-Expression Gradients Underlie Prominent Heterogeneity of CA1 Pyramidal Neurons. *Neuron* **89**, 351-368 (2016). https://doi.org:10.1016/j.neuron.2015.12.013

34 Huszar, R., Zhang, Y., Blockus, H. & Buzsaki, G. Preconfigured dynamics in the hippocampus are guided by embryonic birthdate and rate of neurogenesis. *Nat Neurosci* **25**, 1201-1212 (2022). https://doi.org:10.1038/s41593-022-01138-x

35 Adam, Y. *et al.* Voltage imaging and optogenetics reveal behaviour-dependent changes in hippocampal dynamics. *Nature* **569**, 413-417 (2019). https://doi.org:10.1038/s41586-019-1166-7

36 Klausberger, T. *et al.* Brain-state- and cell-type-specific firing of hippocampal interneurons in vivo. *Nature* **421**, 844-848 (2003). https://doi.org:10.1038/nature01374

37 Wilson, M. A. & McNaughton, B. L. Dynamics of the hippocampal ensemble code for space. *Science* **261**, 1055-1058 (1993).

38 Frank, L. M., Stanley, G. B. & Brown, E. N. Hippocampal plasticity across multiple days of exposure to novel environments. *J Neurosci* **24**, 7681-7689 (2004). https://doi.org:10.1523/JNEUROSCI.1958-04.2004

39 Leutgeb, S., Leutgeb, J. K., Treves, A., Moser, M. B. & Moser, E. I. Distinct ensemble codes in hippocampal areas CA3 and CA1. *Science* **305**, 1295-1298 (2004). https://doi.org:10.1126/science.1100265

40 Nitz, D. & McNaughton, B. Differential modulation of CA1 and dentate gyrus interneurons during exploration of novel environments. *J Neurophysiol* **91**, 863-872 (2004). https://doi.org:10.1152/jn.00614.2003

41 Karlsson, M. P. & Frank, L. M. Network dynamics underlying the formation of sparse, informative representations in the hippocampus. *J Neurosci* **28**, 14271-14281 (2008). https://doi.org:10.1523/JNEUROSCI.4261-08.2008

42 Jeewajee, A., Lever, C., Burton, S., O'Keefe, J. & Burgess, N. Environmental novelty is signaled by reduction of the hippocampal theta frequency. *Hippocampus* **18**, 340-348 (2008). https://doi.org:10.1002/hipo.20394

43 Grosmark, A. D. & Buzsaki, G. Diversity in neural firing dynamics supports both rigid and learned hippocampal sequences. *Science* **351**, 1440-1443 (2016). https://doi.org:10.1126/science.aad1935

44 Grosmark, A. D., Long, J. & Buzsáki, G. r. Recordings from hippocampal area CA1, PRE, during and POST novel spatial learning. *CRCNS. org* **10**, K0862DC0865 (2016).

45 Rolotti, S. V. *et al.* Local feedback inhibition tightly controls rapid formation of hippocampal place fields. *Neuron* **110**, 783-794 e786 (2022). https://doi.org:10.1016/j.neuron.2021.12.003

46 Sheffield, M. E. J., Adoff, M. D. & Dombeck, D. A. Increased Prevalence of Calcium Transients

994 across the Dendritic Arbor during Place Field Formation. *Neuron* **96**, 490-504 e495 (2017).
995 https://doi.org:10.1016/j.neuron.2017.09.029
996 47 Takacs, V. T., Klausberger, T., Somogyi, P., Freund, T. F. & Gulyas, A. I. Extrinsic and local
997 glutamatergic inputs of the rat hippocampal CA1 area differentially innervate pyramidal cells
998 and interneurons. *Hippocampus* **22**, 1379-1391 (2012). https://doi.org:10.1002/hipo.20974
999 48 English, D. F. *et al.* Pyramidal Cell-Interneuron Circuit Architecture and Dynamics in
1000 Hippocampal Networks. *Neuron* **96**, 505-520 e507 (2017).
1001 https://doi.org:10.1016/j.neuron.2017.09.033
1002 49 Maccaferri, G., Roberts, J. D., Szucs, P., Cottingham, C. A. & Somogyi, P. Cell surface domain
1003 specific postsynaptic currents evoked by identified GABAergic neurones in rat hippocampus
1004 in vitro. *J Physiol* **524 Pt 1**, 91-116 (2000). https://doi.org:10.1111/j.1469-7793.2000.t01-3-
1005 00091.x
1006 50 Geiller, T. *et al.* Local circuit amplification of spatial selectivity in the hippocampus. *Nature* **601**,
1007 105-109 (2022). https://doi.org:10.1038/s41586-021-04169-9
1008 51 Trouche, S. *et al.* Recoding a cocaine-place memory engram to a neutral engram in the
1009 hippocampus. *Nat Neurosci* **19**, 564-567 (2016). https://doi.org:10.1038/nn.4250
1010 52 Go, M. A. *et al.* Place Cells in Head-Fixed Mice Navigating a Floating Real-World Environment.
1011 *Front Cell Neurosci* **15**, 618658 (2021). https://doi.org:10.3389/fncel.2021.618658
1012 53 Kramis, R., Vanderwolf, C. H. & Bland, B. H. Two types of hippocampal rhythmical slow activity
1013 in both the rabbit and the rat: relations to behavior and effects of atropine, diethyl ether,
1014 urethane, and pentobarbital. *Exp Neurol* **49**, 58-85 (1975). https://doi.org:10.1016/0014-
1015 4886(75)90195-8
1016 54 Bland, B. H. The physiology and pharmacology of hippocampal formation theta rhythms. *Prog*
1017 *Neurobiol* **26**, 1-54 (1986). https://doi.org:10.1016/0301-0082(86)90019-5
1018 55 Buzsaki, G. Theta oscillations in the hippocampus. *Neuron* **33**, 325-340 (2002).
1019 https://doi.org:10.1016/s0896-6273(02)00586-x
1020 56 Sainsbury, R. S., Heynen, A. & Montoya, C. P. Behavioral correlates of hippocampal type 2 theta
1021 in the rat. *Physiol Behav* **39**, 513-519 (1987). https://doi.org:10.1016/0031-9384(87)90382-9
1022 57 Sainsbury, R. S. Hippocampal theta: a sensory-inhibition theory of function. *Neurosci Biobehav*
1023 *Rev* **22**, 237-241 (1998). https://doi.org:10.1016/s0149-7634(97)00011-0
1024 58 Barry, C., Heys, J. G. & Hasselmo, M. E. Possible role of acetylcholine in regulating spatial
1025 novelty effects on theta rhythm and grid cells. *Front Neural Circuits* **6**, 5 (2012).
1026 https://doi.org:10.3389/fncir.2012.00005
1027 59 Nakajima, Y., Nakajima, S., Leonard, R. J. & Yamaguchi, K. Acetylcholine raises excitability by
1028 inhibiting the fast transient potassium current in cultured hippocampal neurons. *Proc Natl*
1029 *Acad Sci U S A* **83**, 3022-3026 (1986). https://doi.org:10.1073/pnas.83.9.3022
1030 60 Markram, H. & Segal, M. Acetylcholine potentiates responses to N-methyl-D-aspartate in the
1031 rat hippocampus. *Neurosci Lett* **113**, 62-65 (1990). https://doi.org:10.1016/0304-

3940(90)90495-u

61 Fraser, D. D. & MacVicar, B. A. Cholinergic-dependent plateau potential in hippocampal CA1 pyramidal neurons. *J Neurosci* **16**, 4113-4128 (1996). https://doi.org:10.1523/JNEUROSCI.16-13-04113.1996

62 Toth, K., Freund, T. F. & Miles, R. Disinhibition of rat hippocampal pyramidal cells by GABAergic afferents from the septum. *J Physiol* **500 (Pt 2)**, 463-474 (1997). https://doi.org:10.1113/jphysiol.1997.sp022033

63 Colgin, L. L. Mechanisms and functions of theta rhythms. *Annu Rev Neurosci* **36**, 295-312 (2013). https://doi.org:10.1146/annurev-neuro-062012-170330

64 Cobb, S. R., Buhl, E. H., Halasy, K., Paulsen, O. & Somogyi, P. Synchronization of neuronal activity in hippocampus by individual GABAergic interneurons. *Nature* **378**, 75-78 (1995). https://doi.org:10.1038/378075a0

65 Stark, E. *et al.* Inhibition-induced theta resonance in cortical circuits. *Neuron* **80**, 1263-1276 (2013). https://doi.org:10.1016/j.neuron.2013.09.033

66 Landfield, P. W., McGaugh, J. L. & Tusa, R. J. Theta rhythm: a temporal correlate of memory storage processes in the rat. *Science* **175**, 87-89 (1972). https://doi.org:10.1126/science.175.4017.87

67 Berry, S. D. & Thompson, R. F. Prediction of learning rate from the hippocampal electroencephalogram. *Science* **200**, 1298-1300 (1978). https://doi.org:10.1126/science.663612

68 Belchior, H., Lopes-Dos-Santos, V., Tort, A. B. & Ribeiro, S. Increase in hippocampal theta oscillations during spatial decision making. *Hippocampus* **24**, 693-702 (2014). https://doi.org:10.1002/hipo.22260

69 Winson, J. Loss of hippocampal theta rhythm results in spatial memory deficit in the rat. *Science* **201**, 160-163 (1978). https://doi.org:10.1126/science.663646

70 Mitchell, S. J., Rawlins, J. N., Steward, O. & Olton, D. S. Medial septal area lesions disrupt theta rhythm and cholinergic staining in medial entorhinal cortex and produce impaired radial arm maze behavior in rats. *J Neurosci* **2**, 292-302 (1982). https://doi.org:10.1523/JNEUROSCI.02-03-00292.1982

71 Mizumori, S. J., Perez, G. M., Alvarado, M. C., Barnes, C. A. & McNaughton, B. L. Reversible inactivation of the medial septum differentially affects two forms of learning in rats. *Brain research* **528**, 12-20 (1990). https://doi.org:10.1016/0006-8993(90)90188-h

72 M'Harzi, M. & Jarrard, L. E. Effects of medial and lateral septal lesions on acquisition of a place and cue radial maze task. *Behav Brain Res* **49**, 159-165 (1992). https://doi.org:10.1016/s0166-4328(05)80160-3

73 Wang, Y., Romani, S., Lustig, B., Leonardo, A. & Pastalkova, E. Theta sequences are essential for internally generated hippocampal firing fields. *Nat Neurosci* **18**, 282-288 (2015). https://doi.org:10.1038/nn.3904

74 McNaughton, N., Ruan, M. & Woodnorth, M. A. Restoring theta-like rhythmicity in rats restores initial learning in the Morris water maze. *Hippocampus* **16**, 1102-1110 (2006). https://doi.org:10.1002/hipo.20235

75 Lee, D. J. *et al.* Medial septal nucleus theta frequency deep brain stimulation improves spatial working memory after traumatic brain injury. *J Neurotrauma* **30**, 131-139 (2013). https://doi.org:10.1089/neu.2012.2646

76 Hasselmo, M. E., Bodelon, C. & Wyble, B. P. A proposed function for hippocampal theta rhythm: separate phases of encoding and retrieval enhance reversal of prior learning. *Neural Comput* **14**, 793-817 (2002). https://doi.org:10.1162/089976602317318965

77 Rutishauser, U., Ross, I. B., Mamelak, A. N. & Schuman, E. M. Human memory strength is predicted by theta-frequency phase-locking of single neurons. *Nature* **464**, 903-907 (2010). https://doi.org:10.1038/nature08860

78 Siegle, J. H. & Wilson, M. A. Enhancement of encoding and retrieval functions through theta phase-specific manipulation of hippocampus. *Elife* **3**, e03061 (2014). https://doi.org:10.7554/eLife.03061

79 McHugh, S. B. *et al.* Offline hippocampal reactivation during dentate spikes supports flexible memory. *Neuron* **112**, 3768-3781 e3768 (2024). https://doi.org:10.1016/j.neuron.2024.08.022

80 Dvorak, D., Chung, A., Park, E. H. & Fenton, A. A. Dentate spikes and external control of hippocampal function. *Cell Rep* **36**, 109497 (2021). https://doi.org:10.1016/j.celrep.2021.109497

81 Farrell, J. S., Hwaun, E., Dudok, B. & Soltesz, I. Neural and behavioural state switching during hippocampal dentate spikes. *Nature* **628**, 590-595 (2024). https://doi.org:10.1038/s41586-024-07192-8

82 Deuchars, J. & Thomson, A. M. CA1 pyramid-pyramid connections in rat hippocampus in vitro: dual intracellular recordings with biocytin filling. *Neuroscience* **74**, 1009-1018 (1996). https://doi.org:10.1016/0306-4522(96)00251-5

83 Caporale, N. & Dan, Y. Spike timing-dependent plasticity: a Hebbian learning rule. *Annu Rev Neurosci* **31**, 25-46 (2008). https://doi.org:10.1146/annurev.neuro.31.060407.125639

84 Markram, H., Lubke, J., Frotscher, M. & Sakmann, B. Regulation of synaptic efficacy by coincidence of postsynaptic APs and EPSPs. *Science* **275**, 213-215 (1997). https://doi.org:10.1126/science.275.5297.213

85 Bi, G. Q. & Poo, M. M. Synaptic modifications in cultured hippocampal neurons: dependence on spike timing, synaptic strength, and postsynaptic cell type. *J Neurosci* **18**, 10464-10472 (1998). https://doi.org:10.1523/JNEUROSCI.18-24-10464.1998

86 Ali, A. B., Deuchars, J., Pawelzik, H. & Thomson, A. M. CA1 pyramidal to basket and bistratified cell EPSPs: dual intracellular recordings in rat hippocampal slices. *J Physiol* **507 (Pt 1)**, 201-217 (1998). https://doi.org:10.1111/j.1469-7793.1998.201bu.x

87 Ali, A. B. & Thomson, A. M. Facilitating pyramid to horizontal oriens-alveus interneurone inputs: dual intracellular recordings in slices of rat hippocampus. *J Physiol* **507 (Pt 1)**, 185-199 (1998). https://doi.org:10.1111/j.1469-7793.1998.185bu.x

88 Engel, A. K., Konig, P., Kreiter, A. K. & Singer, W. Interhemispheric synchronization of oscillatory neuronal responses in cat visual cortex. *Science* **252**, 1177-1179 (1991). https://doi.org:10.1126/science.252.5009.1177

89 Alonso, J. M., Usrey, W. M. & Reid, R. C. Precisely correlated firing in cells of the lateral geniculate nucleus. *Nature* **383**, 815-819 (1996). https://doi.org:10.1038/383815a0

90 Zheng, Q. *et al.* Rational Design of Fluorogenic and Spontaneously Blinking Labels for Super-Resolution Imaging. *ACS Cent Sci* **5**, 1602-1613 (2019). https://doi.org:10.1021/acscentsci.9b00676

91 Pologruto, T. A., Sabatini, B. L. & Svoboda, K. ScanImage: flexible software for operating laser scanning microscopes. *Biomed Eng Online* **2**, 13 (2003). https://doi.org:10.1186/1475-925X-2-13

92 Huang, Y. C. *et al.* Dynamic assemblies of parvalbumin interneurons in brain oscillations. *Neuron* **112**, 2600-2613 e2605 (2024). https://doi.org:10.1016/j.neuron.2024.05.015

93 Abdelfattah, A. S. *et al.* Bright and photostable chemigenetic indicators for extended in vivo voltage imaging. *Science* **365**, 699-704 (2019). https://doi.org:10.1126/science.aav6416

Acknowledgments

We express our sincere gratitude to Dr. Luke Lavis for sharing the JF_{552}-HaloTag ligand. Special thanks to Mr. Yu-Ting Lin and Ms. Hui-Ching Chen for technical assistance. We are grateful to Drs. Shih-Chieh Lin, Kuo-Hua Huang, Shi-Bing Yang, and Fu-Chin Liu for their insightful comments on the manuscript.

Funding statements

National Science and Technology Council, Taiwan (B.-J.L. and T.-W.C.)
Howard Hughes Medical Institute, USA (E.R.S.)

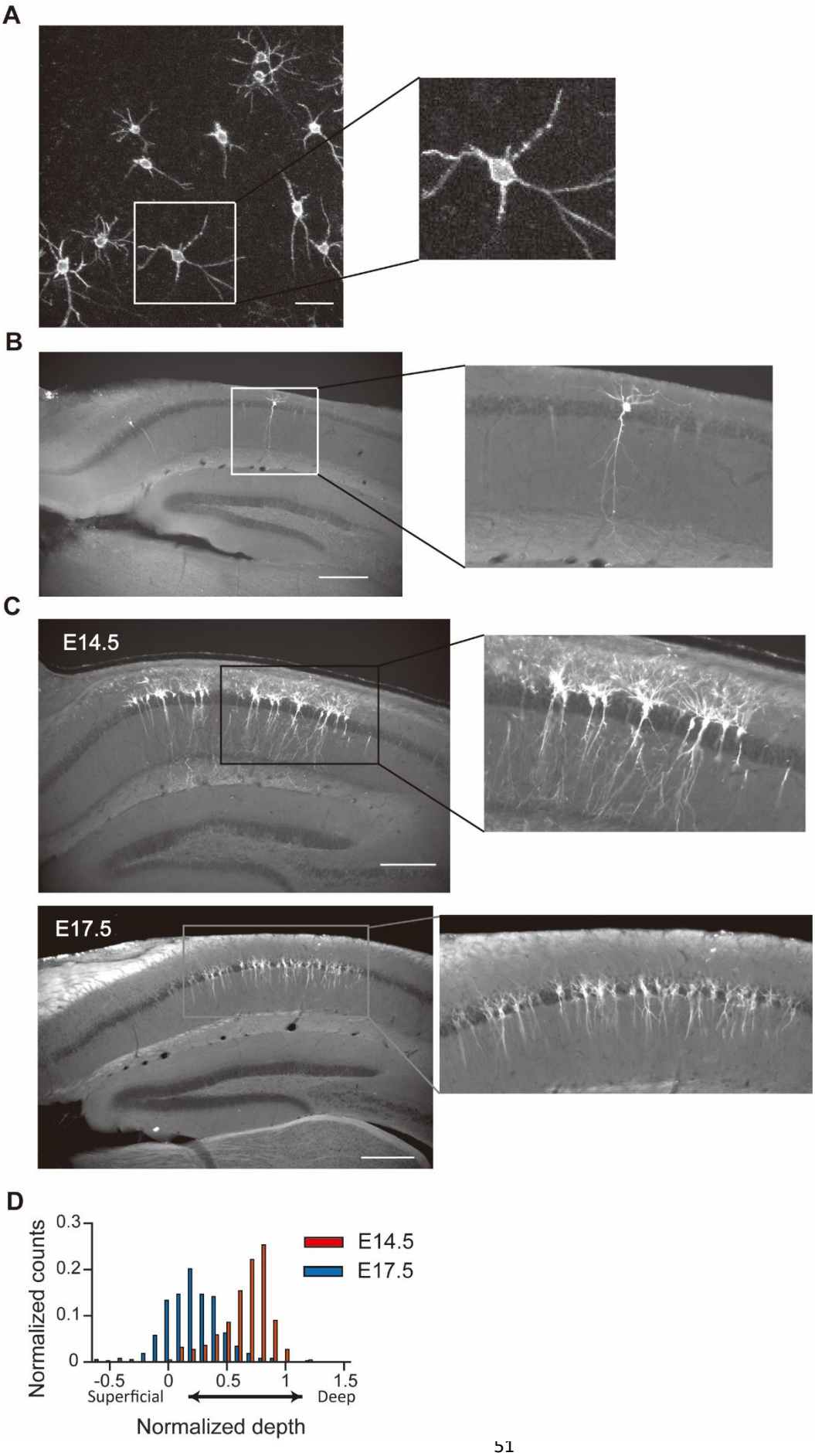
A
B
C
E14.5
E17.5
D
Normalized counts
0.3
0.2
0.1
0
-0.5
0
0.5
1
1.5
Superficial
Deep
Normalized depth
E14.5
E17.5

1137

1138 **Supplementary Figure 1. Morphology of Voltron-expressing neurons and their positions along the**

1139 **deep-superficial axis.**

1140 **(A)** Two-photon z-stack maximum intensity projection images of Voltron-expressing neurons

1141 obtained after imaging experiments. These neurons exhibit well-preserved membrane and dendritic

1142 morphology. Scale bars: 50 μ m.

1143 **(B)** Post-hoc histological images of a sparsely labeled neuron previously subjected to voltage

1144 imaging. Scale bars: 300 μ m.

1145 **(C)** Micrographs of labeled neurons from *in-utero* electroporation at embryonic day 14.5 (E14.5;

1146 upper panel) and E17.5 (lower panel). Scale bars: 300 μ m.

1147 **(D)** Histograms of normalized depths for E14.5 neurons (red) and E17.5 neurons (blue). A higher

1148 normalized depth indicates that the soma is located deeper within the pyramidal layer. Normalized

1149 depths for E14.5 neurons are significantly higher than those for E17.5 neurons ($t_{(601)}$=22.8,

1150 p<0.0001, Student's t-test).

1151

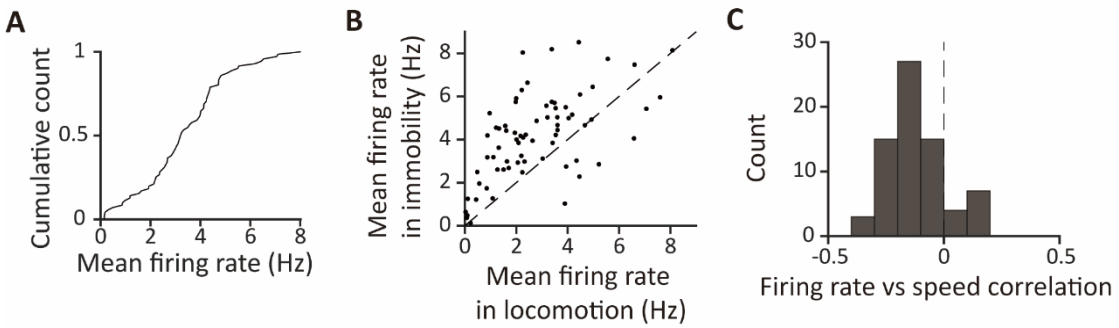

Supplementary Figure 2. Mean firing rate distribution and correlation with animals' speed.

(A) Cumulative distribution of mean firing rates averaged throughout the entire 180-second recording period.

(B) Mean firing rates during locomotion plotted against mean firing rates during immobility for individual cells. Each dot represents a cell. Mean firing rates are higher during immobility than during locomotion (4.2±0.2 Hz for immobility, 2.8±0.2 Hz for locomotion, $t_{(70)}$=6.63, p<0.0001, Student's t-test).

(C) Histogram of correlation coefficients between instantaneous firing rates and the animals' speed for each neuron.

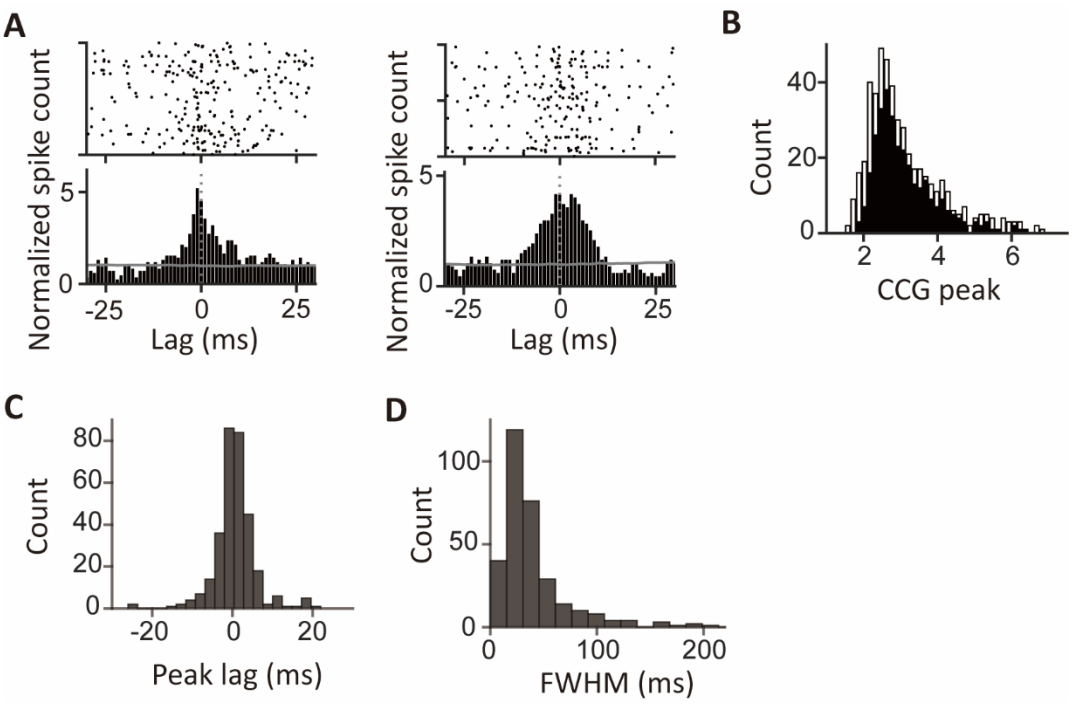

1163

1164 **Figure 1-figure supplement 1. Pairwise cross-correlogram (CCG) between CA1 pyramidal cells.**

1165 **(A)** CCGs of two representative cell pairs exhibiting significant peaks compared to the jittered spike

1166 trains of the target cells (gray lines).

1167 **(B)** Distribution of the CCG peaks (*n*=497 pairs). Black: CCG peaks with significance ($p<0.05$). White:

1168 CCG peaks without significance ($p>=0.05$).

1169 **(C)** Histogram of peak lags of significant CCG peaks (*n*=315 pairs).

1170 **(D)** Histogram of FWHMs of significant CCG peaks (*n*=315 pairs).

1171

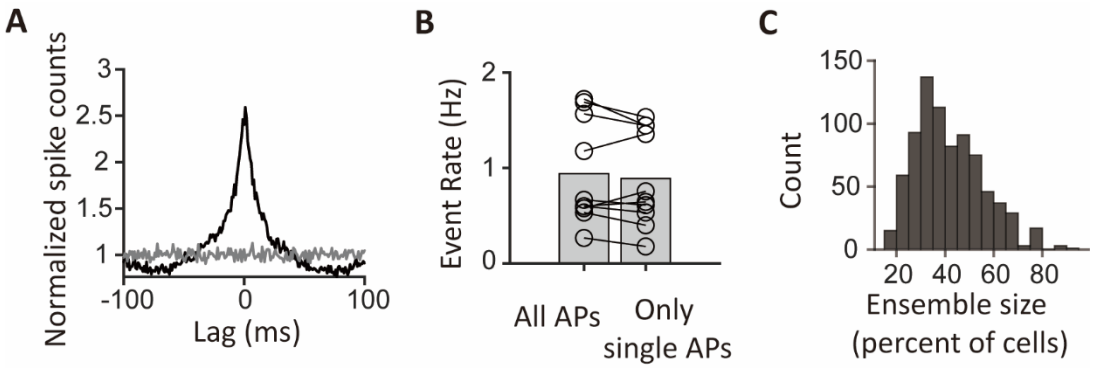

Supplementary Figure 3. Population synchrony remains after removing the later spikes in bursts.

(A) Grand-average cross-correlogram (CCG) calculated using spike trains with the later spikes in bursts removed. The gray line represents the mean grand-average CCG between reference cells and randomly selected cells from different sessions.

(B) Pairwise comparison of population synchrony event rates between spike trains containing all spikes and those with the later spikes in bursts removed. Bar heights represent group means (*n*=10 segments, *p*=0.36, Wilcoxon signed-rank test).

(C) Histogram of ensemble sizes showing the percentage of cells participating in synchronous ensembles.

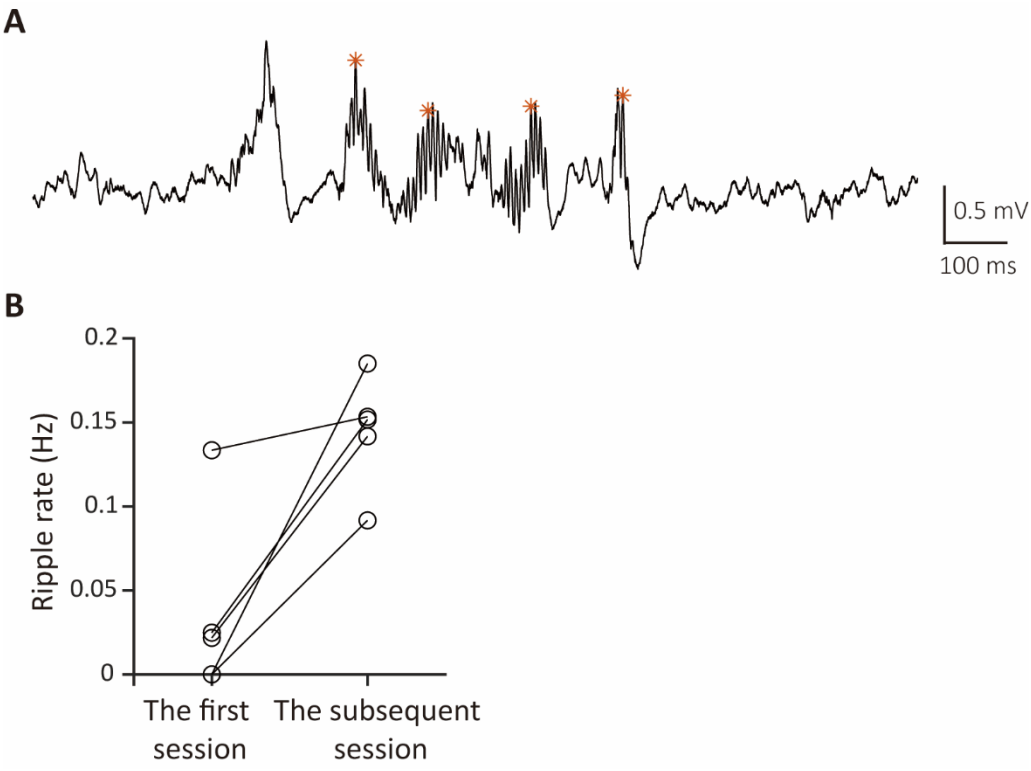

Figure 3-figure supplement 1. LFP ripples recorded in the first and subsequent sessions in a novel maze.

(A) An example LFP trace with ripples recorded in a subsequent session following the first session of novel exploration, where no ripple was detected.

(B) Ripple rates in the first and subsequent sessions recorded in the same animals (n=5 mice) during novel exploration.

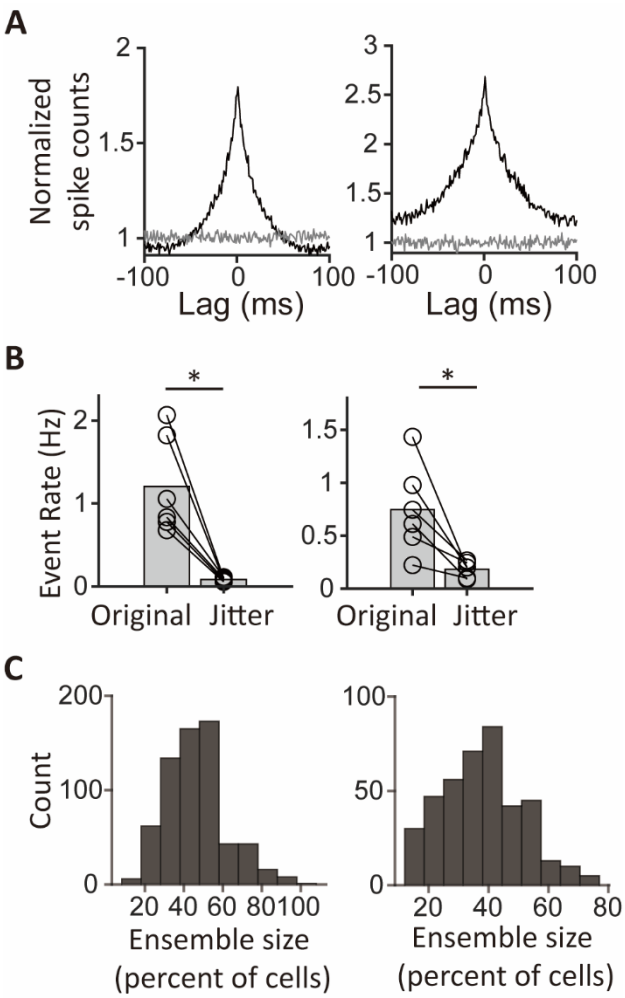

Figure 3-figure supplement 2. Population synchrony during novel immobility.

(A) Grand average cross-correlograms (CCGs) for neurons labeled on E14.5 (left) and on E17.5 (right). The gray line represents the mean grand-average CCG between reference cells and randomly selected cells from different sessions.

(B) Pairwise comparison of synchronous event rates between the original and jittered data. Event rates were significantly higher in the original data compared to jittered controls for E14.5 neurons (left; mean event rate: 1.21 ± 0.24 Hz for the original data, 0.08 ± 0.009 Hz for jittered data, n=6 segments, W=21, p=0.03, Wilcoxon signed-rank test) and E17.5 neurons (right; mean event rate: 0.75 ± 0.17 Hz for the original data, 0.18 ± 0.03 Hz for jittered data, n=6 segments, W=21, p=0.03, Wilcoxon signed-rank test). Bar heights represent group means. *p<0.05

(C) Histograms of ensemble sizes showing the percentage of cells participating in synchronous ensembles for E14.5 neurons (left) and E17.5 neurons (right).

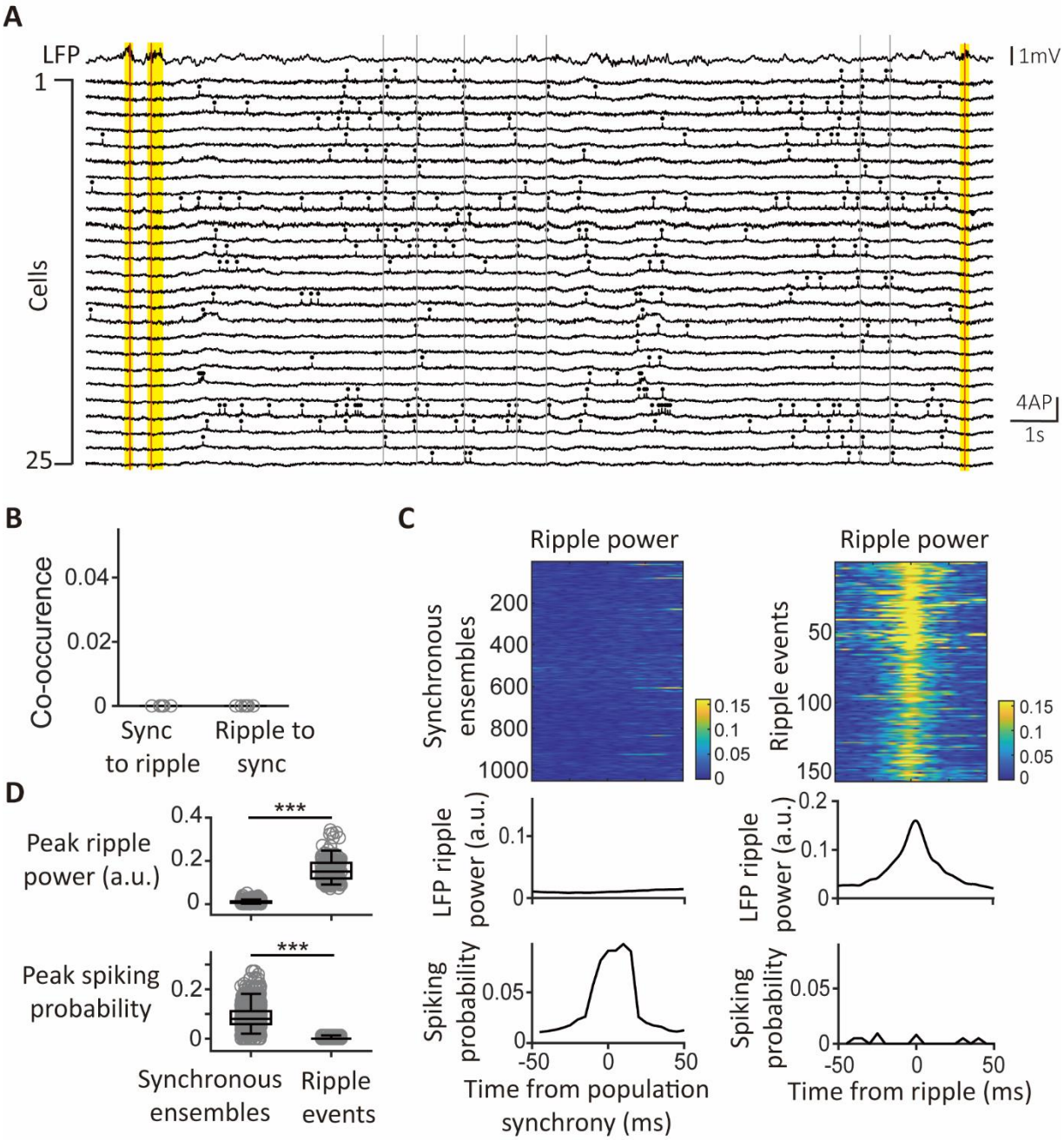

Figure 3-figure supplement 3. Population synchrony outside ripple episodes during novel immobility.

(A) Example traces illustrating the distinct timings of ripple episodes and synchronous ensembles. Top: Simultaneously recorded LFP trace showing episodes of ripple oscillations. Red vertical lines indicate the timings of peak ripple power in the LFP trace, while yellow vertical bars mark the duration of ripple episodes. Bottom: Fluorescence traces from 25 CA1PCs. Gray vertical lines indicate the timings of synchronous ensembles.

(B) Percentages of co-occurrence between synchronous ensembles and ripple events. The “sync to ripples” group represents the percentage of ripple events that co-occur with synchronous ensembles, while the “ripples to sync” group shows the percentage of synchronous ensembles that co-occur with ripple events. Each gray circle represents an individual session.

(C) LFP ripple power and spiking probability aligned to synchronous ensembles and ripple events. **Upper panel**: Color-coded LFP power at ripple frequency (120-240Hz), aligned to the timings of 1052 synchronous ensembles (left) and 174 ripple events (right). **Middle panel**: Average LFP power at ripple frequencies aligned to the timings of synchronous ensembles (left) and ripple events (right). **Lower panel**: Average spiking probability of all recorded cells aligned to the timings of synchronous ensembles (left) and ripple events (right).

(D) Boxplots and comparisons of peak ripple power (upper panel) and peak spiking probability (lower panel) at the timings (t=0) of population synchrony (left) and ripple events (right). For peak ripple power: $p<0.001$, $t_{(1224)}=86.6$, Student’s *t*-test; for peak spiking probability: $p<0.001$, $t_{(1224)}=24.3$, Student’s *t*-test. Gray circles indicate peak values for individual triggered traces.

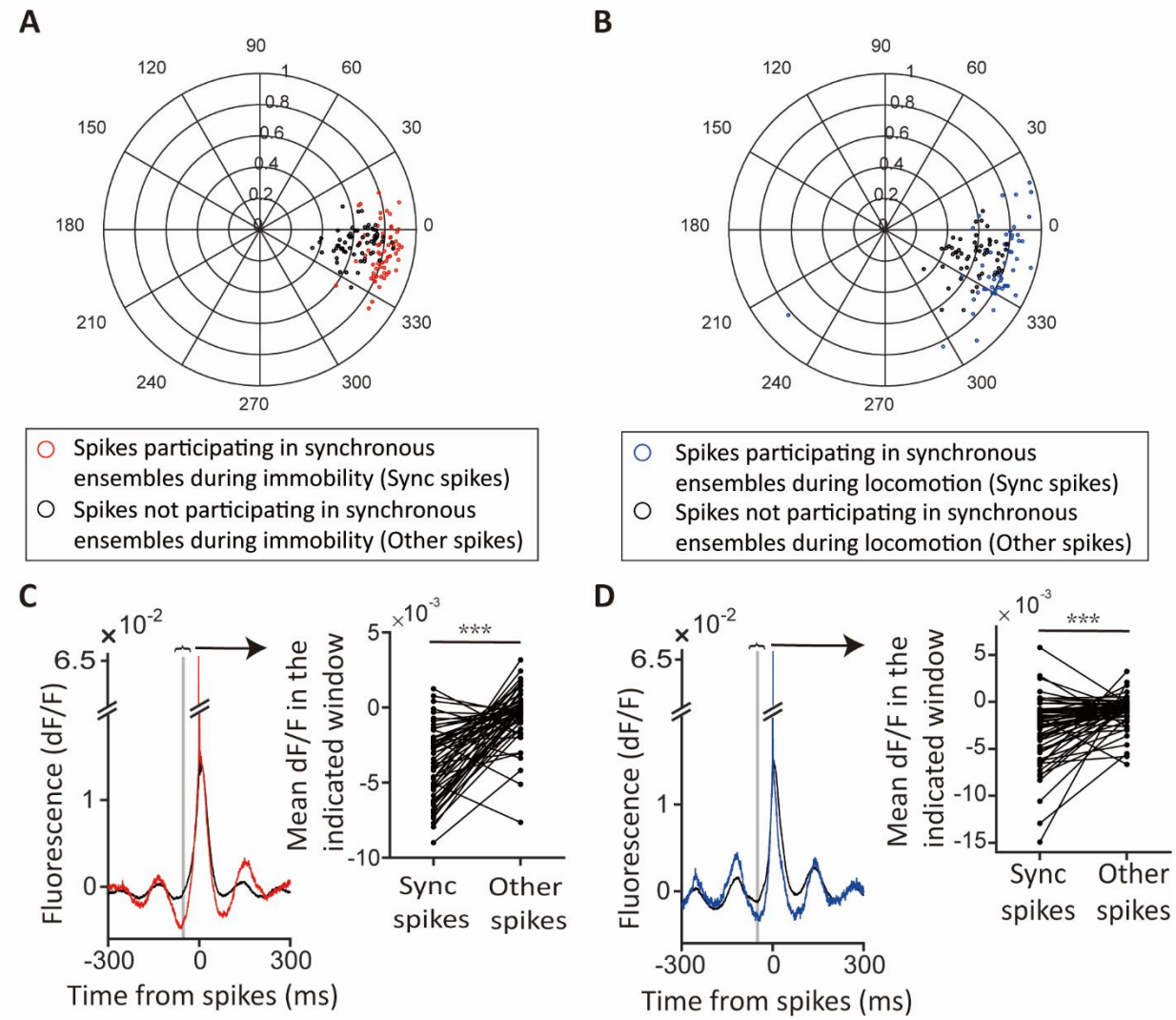

Figure 5-figure supplement 1. SubVm theta modulation of spikes during immobility and locomotion periods of novel exploration.

(A) Polar plot comparing subVm theta modulation between spikes participating in synchronous ensembles (sync spikes) and spikes not participating in synchronous ensembles (other spikes) during immobility. Each dot represents the averaged modulation of a cell. Cells with modulation strengths that are not significant are excluded in the plot and in the comparison. The modulation strengths of spikes participating in synchrony are significantly higher than those of spikes not participating in synchrony (modulation strength for spikes participating in synchronous ensembles: 0.81±0.07, for spikes not participating in synchronous ensembles: 0.64±0.11, mean±s.d., $t_{(64)}$=12.6, p<0.001, pair Student's t-test).

1239 **(B)** Same as in (A), but during locomotion (modulation strength for spikes participating in
1240 synchronous ensembles: 0.80±0.09, for spikes not participating in synchronous ensembles: 0.60±
1241 0.12, mean±s.d., $t_{(53)}$=12.3, p<0.001, pair Student's t-test).
1242 **(C)** Average fluorescence triggered by cells' spikes participating in synchronous ensembles (red, sync
1243 spikes) and not participating in synchronous ensembles during immobility (black, other spikes; n=59
1244 cells). Inset: Pairwise comparison of average fluorescence 50±5 ms before time of spikes (t=0)
1245 between the two triggered groups (n=59 cells, p<0.001, pair Student's t-test). ***p<0.001.
1246 **(D)** Same as in (C), but during locomotion. Inset: Pairwise comparison of average fluorescence (n=59
1247 cells, p<0.001, pair Student's t-test).
1248

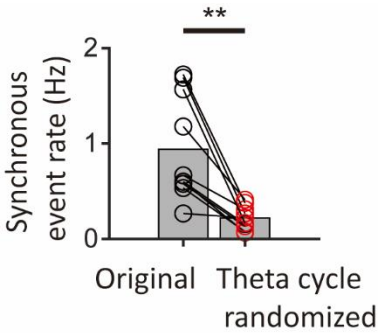

Supplementary Figure 4. Significant reduction of population synchrony by randomizing spikes across theta cycles while preserving phases

Pairwise comparison of population synchrony event rates between the original spike trains and randomized spike trains, in which spike timings were shuffled across theta cycles while preserving phases (*n*=10 segments, *p*=0.002, Wilcoxon signed-rank test). Bar heights represent group means.

** *p*<0.01

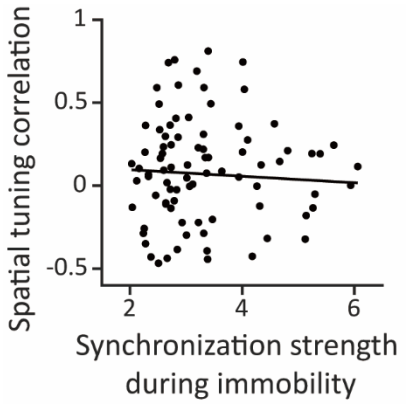

Figure 5-figure supplement 1. Synchronization strengths during immobility show little correlation with the similarity of spatial tunings between place cells. Synchronization strengths during immobility plotted against correlation coefficients of spatial tunings for pairs of place cells. Synchronization strengths show little correlation with similarities of spatial tunings (Spearman correlation coefficient=-0.003, p=0.98, n=88 cell pairs).

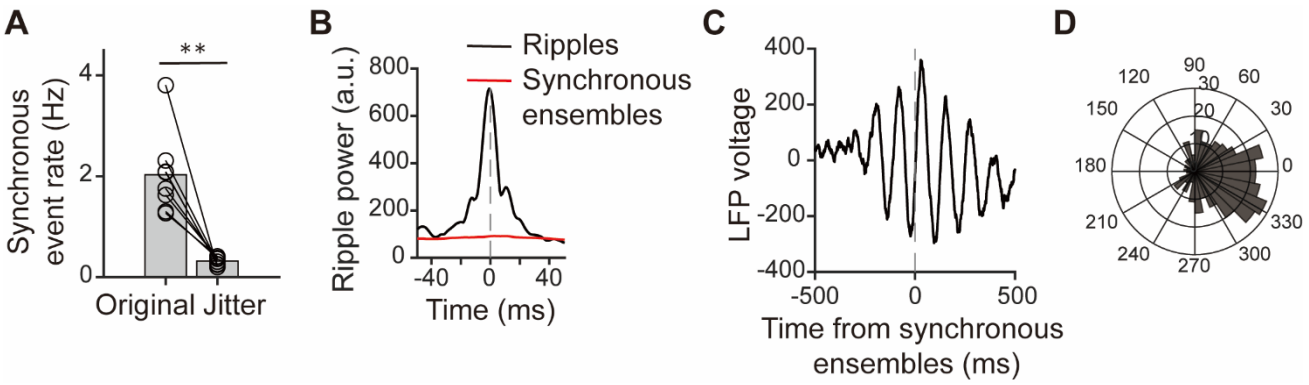

Supplementary Figure 5. Analyses of synchronous ensembles in the publicly available data

(A) Pairwise comparison of synchronous event rates between the original and jittered data. Event rates were significantly higher in the original data compared to jittered controls (n=8 sessions, p=0.008, Wilcoxon signed-rank test). Bar heights represent group means. **p<0.01.

(B) Dynamics of ripple power aligned to timings of ripples (black) and timings of synchronous ensembles (red).

(C) Average LFP trace aligned to timings of synchronous ensembles of a session.

(D) Polar histogram of the differences between theta phases of individual synchronous ensembles and the preferred phase of the session.